

2012-01-01

Investigation Of Gas-Solid Fluidized Bed With Non-Spherical Particles

Mario Alberto Ruvalcaba

University of Texas at El Paso, mruvalcaba@miners.utep.edu

Follow this and additional works at: https://digitalcommons.utep.edu/open_etd



Part of the [Civil Engineering Commons](#), and the [Oil, Gas, and Energy Commons](#)

Recommended Citation

Ruvalcaba, Mario Alberto, "Investigation Of Gas-Solid Fluidized Bed With Non-Spherical Particles" (2012). *Open Access Theses & Dissertations*. 2182.

https://digitalcommons.utep.edu/open_etd/2182

This is brought to you for free and open access by DigitalCommons@UTEP. It has been accepted for inclusion in Open Access Theses & Dissertations by an authorized administrator of DigitalCommons@UTEP. For more information, please contact lweber@utep.edu.

INVESTIGATION OF GAS-SOLID FLUIDIZED BED WITH NON-SPHERICAL PARTICLES

MARIO A. RUVALCABA

Environmental Science and Engineering Doctoral Program

APPROVED:

Ahsan Choudhuri, Ph.D., Chair

Norman Love, Ph.D.

Vinod Kumar, Ph.D.

Evgeny Shafirovich, Ph.D.

Jose Espiritu, Ph.D.

Benjamin C. Flores, Ph.D.
Interim Dean of the Graduate School

Copyright ©

by

Mario A. Ruvalcaba

2012

Dedication

To my family

INVESTIGATION OF GAS-SOLID FLUIDIZED BED WITH NON-
SPHERICAL PARTICLES

by

MARIO A. RUVALCABA, M.S.M.E.

DISSERTATION

Presented to the Faculty of the Graduate School of

The University of Texas at El Paso

in Partial Fulfillment

of the Requirements

for the Degree of

DOCTOR OF PHILOSOPHY

Environmental Science and Engineering Doctoral Program

THE UNIVERSITY OF TEXAS AT EL PASO

May 2012

Acknowledgements

Perhaps the most direct support to my work has come from my advisor Dr. Ahsan Choudhuri (Mechanical Engineering Department, University of Texas at El Paso). I thoroughly appreciated his patient guidance throughout this project. He helped me work in the area of my research interest in computational fluid dynamics and energy systems. His work ethic provides a great example for all the students in our group. He was also been very understanding as I went through some of the hardest times in my life and for that I am very thankful.

I would like to thank my thesis committee members, Dr. Norman Love, Dr. Vinod Kumar and Dr. Evgeny Shafirovich for being in the committee and for their cooperation and suggestions.

Thanks to the financial support from the Department of Energy (DOE) and the use of the MFI_X (Multiphase Flow with Interphase eXchanges) code.

Thanks to all my wonderful friends at UTEP for being there for me at all times. Also, my sincere thanks to all my teachers who have been part of my academic career.

Finally, my acknowledgments would be incomplete if I did not include my family. With the no exception any of them even know exactly what it is I do, but I could never have done it without them. My parents have encouraged me since childhood and always given me a reason to do my best. All of my accomplishments are enabled by the support of my family.

Abstract

The number of experimental and numerical studies of multiphase flows has remarkably increased over the last several years. This research has abundant applications in energy, chemical, and conversion processes. Common use of these technologies includes catalytic cracking for petroleum refineries, fluidized bed reactors (type of chemical reactor), interface modification, and has been an important technology breakthrough in coal gasification. The present work will concentrate on the investigation and validation of gas-solid flows utilizing numerical methods. The gas-solid flows study on this research assumes the solid and gas phases as continua with averaged properties.

The fluid flow computation was achieved using two different solvers: 1) FLUENT a general-purpose CFD code based on the finite volume method on a collocated grid. FLUENT technology offers a wide array of physical models that can be applied to a wide array of industries, 2) MFI (Multiphase Flow with Interphase eXchanges) a solver developed at the Department of Energy's National Energy Technology Laboratory (NETL) for multiphase flows. MFI is a general-purpose hydrodynamic model that describes chemical reactions and heat transfer in dense or dilute fluid-solids flows, typical in energy conversion and chemical processing reactors. MFI calculations give detailed information on pressure, temperature, composition, and velocity distributions.

Table of Contents

Acknowledgements.....	v
Abstract.....	vi
Table of Contents.....	vii
List of Tables	ix
List of Figures.....	x
Chapter 1: Introduction.....	1
1.1 An Overview on Gas-Solid Flows.....	1
1.2 Understanding the Behavior of Multiphase Flow Fluidized Beds.....	2
1.3 Fluidization of Particles.....	4
1.4 Approach to Model Gas-Solid Flows.....	7
1.5 Gas-Solid Flows with Non-Spherical Particles.....	7
Chapter 2: Literature Review.....	9
2.1 Eulerian-Eulerian Models.....	9
2.2 Eulerian-Lagrangian Models.....	9
2.3 Non-Spherical Particles Research.....	10
2.4 Overview of Current Work.....	13
2.5 Practical Relevance.....	13
2.5.1 Gasification Processes.....	14
Chapter 3: Objectives.....	17
Chapter 4: Fluidization.....	18
4.1 Fluidized Bed Behavior.....	18
4.2 Bed Pressure Drop.....	19
4.3 Flow Modeling.....	19
4.4 Theoretical Determination of Minimum Fluidization Velocity	23
Chapter 5: Simulation Phase Models.....	26
5.1 Gas-Phase Governing Equations.....	26
5.1.1 Volume Fraction Equation.....	26
5.1.2 Continuity Equation.....	26

5.1.3	Momentum Equation.....	26
5.2	Drag Correlations.....	27
5.2.1	Syamlal-O'Brien Correlation.....	27
5.2.2	Gidaspow Correlation.....	28
5.3	Solid-Phase Governing Equations.....	29
5.3.1	Continuity Equation.....	29
5.3.2	Momentum Equation.....	30
5.4	Modeling Turbulence: The k- ϵ model	31
Chapter 6:	Fluidized Bed Simulation.....	32
6.1	Spherical Particles Modeling.....	33
6.2	Non-Spherical Particles Modeling.....	35
6.2.1	Literature Non-Spherical Drag Correlation.....	35
6.2.2	Single Non-Spherical Particle Drag Analysis.....	37
a)	Numerical Modeling.....	39
6.2.3	Experimental Non-Spherical Drag Correlation.....	42
6.3	Theoretical Correlation Validation.....	43
Chapter 7:	Experimental Setup.....	44
7.1	Spherical and Non-Spherical Particles.....	44
7.2	Single Non-Spherical Particle Analysis and Non-Spherical Drag Correlation.....	47
Chapter 8:	Results and Discussion.....	49
8.1	Spherical Particles.....	49
8.2	Non-Spherical Particles.....	55
8.2.1	Literature Drag Correlation.....	55
8.2.2	Single Non-Spherical Particle Analysis.....	60
A.	Numerical.....	60
B.	Experimental.....	62
8.2.3	Experimental Non-Spherical Drag Correlation.....	62
Chapter 9:	Conclusions.....	70
References.....		73
Appendix.....		81
Vita.....		90

List of Tables

Table 1: Geldart's Classification of Particles.....	6
Table 2: Basic Form of Correlations for Re_{mf} Derived from Pressure Drop Principles.....	25
Table 3: Borosilicate glass physical properties.....	34
Table 4: MFIx simulation parameters.....	35
Table 5: Numerical, theoretical and experimental results for spherical particles.....	52
Table 6: Non-spherical numerical, theoretical and experimental results.....	57
Table 7: Numerical and experimental results comparison.....	62
Table 8: Non-spherical numerical, theoretical and experimental results.....	66
Table 9: User Defined Function for Syamlal-Obrien with Holzer and Sommerfeld Drag Correlation....	81
Table 10: User Defined Function for Syamlal-Obrien Corrected with Experimentally Developed Drag Correlation.....	83
Table 11: MFIx DAT File Example.....	85
Table 12: Experimental Drag Coefficient and Reynolds Number Data.....	87

List of Figures

Figure 1.1: Fluidized Bed Schematic.....	4
Figure 1.2: Geldart Classification of Powders.....	5
Figure 2.1: Fluidized Bed Gasifier.....	15
Figure 2.2: Entrained Flow Gasifier.....	16
Figure 4.1: Bed Performance with Respect to the Gas Velocity.....	18
Figure 6.1: a) Particle Bed Setup b) MFIX analysis sections.....	33
Figure 6.2: Actual photograph showing sphericity analysis of a non-spherical particle.....	36
Figure 6.3: Non-spherical geometric approximation: a) particle used, b) ellipsoid.....	38
Figure 6.4: Grid domain and boundary conditions.....	40
Figure 6.5: Grid with particle rectangular-constant-size quad elements region.....	41
Figure 6.6: Grid with particle elliptical-constant-size quad elements region.....	41
Figure 7.1: Fluidized bed experimental setup.....	45
Figure 7.2: a) High-speed particle motion b) Magnified photographs of spherical particles, and non-spherical particles.....	46
Figure 7.3: Experimental setup.....	48
Figure 7.4: Particle motion captured with high-speed camera.....	48
Figure 8.1: FLUENT spherical particles validation with experimental results.....	50
Figure 8.2: MFIX spherical particles validation with experimental results.....	51
Figure 8.3: Snapshots of gas-axial velocity at 75 cm/s inflow velocity with spherical particles.....	53
Figure 8.4: Snapshots of solids velocity vector-field for inflow velocity of 75 cm/s with spherical Particles.....	53
Figure 8.5: Snapshots of solid-phase vol. fraction for inflow velocity of 75 cm/s with spherical particles.....	54
Figure 8.6: Comparison of snapshots of bubbling behavior of spherical particles among simulation (top row) and experiment (bottom row) at $t = 2, 5, 7$ s from left to right.....	55
Figure 8.7: Non-spherical particles fluidization curves from simulations results, theoretical approximation and experimental predictions.....	56
Figure 8.8: Snapshots of gas-axial velocity at 75 cm/s inflow velocity with non-spherical particles.....	58
Figure 8.9: Snapshots of solids velocity vector-field for inflow velocity of 75 cm/s with non-spherical particles.....	58
Figure 8.10: Snapshots of solid-phase vol. fraction for inflow velocity of 75 cm/s with non-spherical particles.....	59
Figure 8.11: Particle velocity results.....	60
Figure 8.12: Velocity contours at different times.....	61
Figure 8.13: Fluid force acting on the particle.....	61
Figure 8.14: Drag coefficient vs. Reynolds number of non-spherical particles with sphericity of 0.55 (105 data points) and its corresponding numerical correlation.....	63
Figure 8.15: Non-spherical particles fluidization curves from simulations results, theoretical approximation and experimental predictions.....	65
Figure 8.16: Snapshots of gas-axial velocity at 75 cm/s inflow velocity with non-spherical particles.....	67
Figure 8.17: Snapshots of solids velocity vector-field for inflow velocity of 75 cm/s with non-spherical particles.....	68
Figure 8.18: Snapshots of solid-phase vol. fraction for inflow velocity of 75 cm/s with non-spherical particles.....	69

Chapter 1: Introduction

1.1 An Overview on Gas-Solid Flows

Theoretical, experimental and numerical studies are being carried out by a variety of research groups to comprehend the gas-solid flow dynamics. Bouillard et al. (1989) used a two fluid model to investigate a fluidized bed with any solid blockages inside the bed. Dasgupta et al. (1997) have developed model for gas-particle flow in a vertical channel. For the solid stress tensor they used the Newtonian model. In such flows, when the particle number increases, the inertial and viscous effects are dominated by the inter-particle collisions. Also a good work in this area may be found in Crowe et al. (1998). Glasser et al. (1998) have performed theoretical studies and computed the solutions for one-dimensional and two-dimensional traveling wave solutions for the equations of motion for gas and particles in a fluidized bed. Glasser et al. used the Newtonian model for the solid stress tensor. Glasser et al. found that the solutions for fully developed two dimensional waves capture the bubble phenomenon in fluidized beds. In fluidized beds regions of high and low particle concentrations are seen to form sporadically. The regions of low particle concentration are known as bubbles and those of high particle concentration are called clusters (Glasser et al., 1998).

Moreover, Detamore et al. (2001) have completed an analysis of scale-up of circulating fluidized beds using kinetic theory. In addition, the modeling of gas-solid flows with combined kinetic theory for the granular phase with continuum representations for the gas phase (Detamore, 2001).

1.2 Understanding the Behavior of Multiphase Flow Fluidized Beds

During the last few decades Computational Fluid Dynamics (CFD) has become a very powerful and versatile tool for the numerical analysis of transport phenomena. With continuously increasing computer power combined with the development of improved physical models CFD has become a very useful tool for chemical engineers. CFD modeling of gas-fluidized beds has proven to be successful and new developments in this area are promising. The majority of studies on modeling of fluidized beds are concerned with the hydrodynamics only. Although attempts have been reported where the hydrodynamics were modeled combined with mass transfer and chemical reaction (Samuelsberg and Hjertager, 1996, Gao et al., 1999) the results of such attempts depend strongly on how well the hydrodynamics are modeled. Kuipers and Swaaij (1998) demonstrated that the predicted performance of a riser reactor in terms of chemical conversion depends strongly on the prevailing flow structure in the riser. The authors showed that if the flow structure is not well captured by the hydrodynamic model a sensible prediction of the reactor performance is impossible. Therefore the development of reliable hydrodynamic models is of utmost importance in order to arrive ultimately at models that are capable of predicting the performance of fluidized beds reactors. Hence, the focus of the present study is on the hydrodynamics of the flow.

Multiphase flows can be classified into four categories: gas-liquid, liquid-solid, gas-solid and three phase flows. In this work gas-solid flow type is investigated. A typical example of a gas-solid flow application is a fluidized bed. Conceptually, this device consists of a vertical vessel containing a bed of particles that may range in size from microns to centimeters. A fluid (frequently a gas) is pumped through the porous bottom of the vessel, and through the bed (Wu, 1997). As the gas velocity is increased, initially increasing pressures drop is observed across the bed. Nevertheless, when the pressure drop reaches a value close to the weight of the bed per unit area, the particles become suspended in the

fluid stream and the bed is said to be fluidized. Numerous flow regimes are normally used to explain the characteristics of the flow through a particle bed, these include:

- Slugging bed: Bubbles of gas occupy entire fragments of the bed containment vessel and layers are created, splitting the bed into sections.
- Boiling bed: A bed in which the gas bubbles are about the same size as the solid particles.
- Channeling bed: A bed in which gas channels are formed where most of the gas flows through.
- Spouting bed: A bed in which a single gas opening is formed in which some particles flow and fall to the outside. (Geldart, 1973)

A typical fluidized bed schematic is shown in Fig. 1.1. In this system, the solid is in the form of particles that are free to move about in the reactor. Fluidized beds provide more efficient contacting between the solid and the fluid and are integral in enabling catalytic cracking to be a practical, industrial-scale process.

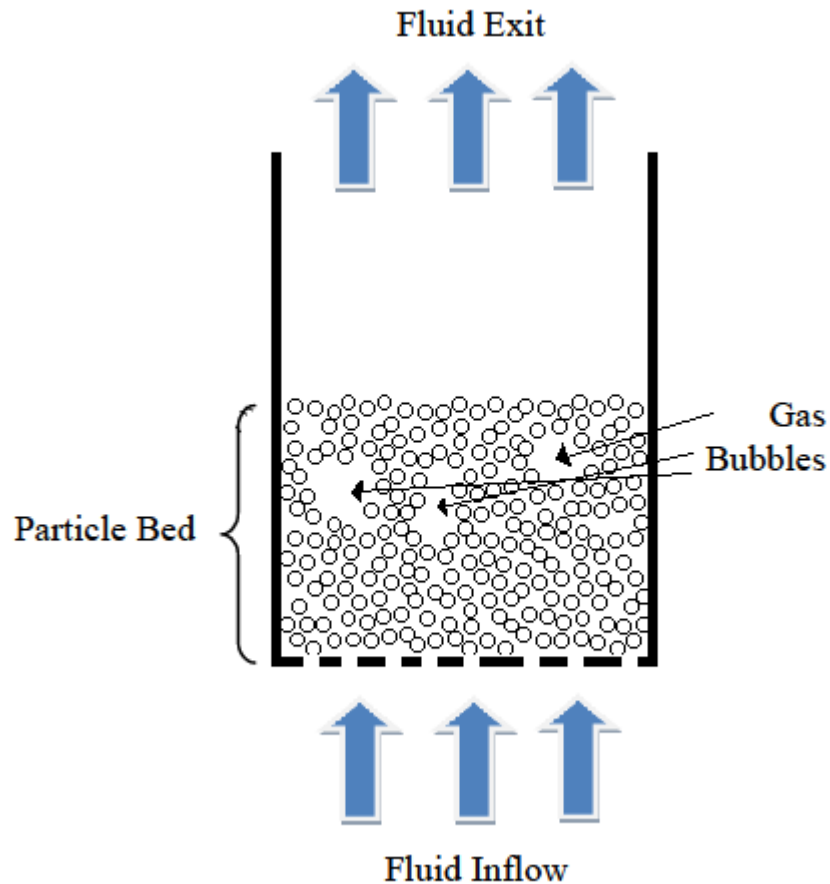


Figure 1.1: Fluidized Bed Schematic

1.3 Fluidization of Particles

In 1973, Professor D. Geldart classified powders that have similar properties into four groups and designated them by the letters A, B, C, and D. This collection is called "Geldart Groups. The groups are defined by their locations on a diagram of solid-fluid density difference ($\rho_s - \rho_f$) and particle size (d_p). Moreover, fluidized bed design methodologies can be customized based upon the particle's Geldart grouping. A mapping of these groups is shown in Figure 1.2 for air fluidized beds (Glasser, 1998).

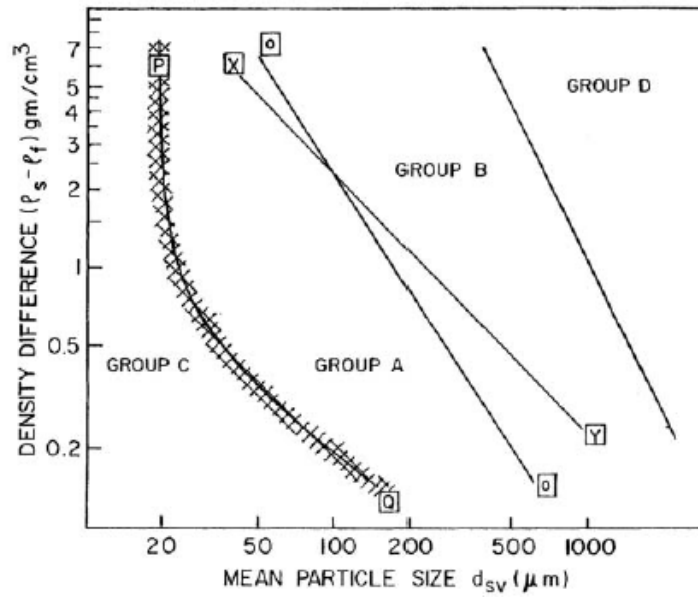


Figure 1.2: Geldart Classification of Powders (Geldart, 1973)

Group A: “Prior to the initiation of a bubbling bed phase, beds from these particles will expand by a factor of 2 to 3 at incipient fluidization, due to a decreased bulk density. Most powder-catalyzed beds utilize this group”.

Group B: “Bubbling typically forms directly at incipient fluidization”.

Group C: “This group contains extremely fine and subsequently the most cohesive particles. These particles fluidize under very difficult to achieve conditions, and may require the application of an external force, such as mechanical agitation”.

Group D: “Fluidization of this group requires very high fluid energies and is typically associated with high levels of abrasion. Roasting coffee beans, gasifying coals, and some roasting metal ores are such solids, and they are usually processed in shallow beds or in the spouting mode” (Geldart, 1973).

Detailed characteristics of powders that belong to the four groups are presented in Table 1.

Table 1: Geldart's Classification of Particles (Gupta and Sathiyamoorthy, 1999).

	Group	
	A	B
Example	Cracking catalyst	Sand
Particle size (d_p), μm	30–100	$40 < d_p < 500$
Density (ρ_s), kg/m^3	< 1400	$1400 \leq \rho_s \leq 4000$
Expansion	Large even before bubbling	Small
Bed collapse rate	Slow (e.g., 0.3–0.6 cm/s)	Very fast
Mixing	Rapid even with a few bubbles	Little in the absence of bubbles
Bubbles	Appear even before U_{mf} (i.e., $U_{mb}/U_{mf} > 1$) Split and recombine frequently Rise velocity $>$ interstitial gas velocity For freely bubbling bed, rise velocity (30–40 cm/s) of small bubble (< 4 cm) not dependent on bubble size Maximum bubble size exists Cloud-to-bubble-volume ratio is negligible	Appear after U_{mf} ($U_{mb}/U_{mf} \approx 1$) Coalescence is predominant Rise velocity $>$ interstitial gas velocity Size increases linearly with bed height and excess gas velocity No evidence Cloud-to-bubble-volume ratio not negligible
Slugs	Slugs produced at high superficial velocity and break Slug size decreases with d_p	Slugs at high velocity of gas, rise along wall and no evidence of breakdown
	Group	
	C	D
Example	Finer	Coarse
Particle size (d_p), μm	$< 60 \mu\text{m}$, if $(\rho_s - \rho_g) < 500 \text{ kg/m}^3$, $< 20 \mu\text{m}$, if $(\rho_s - \rho_g) > 1000 \text{ kg/m}^3$	> 500
Density (ρ_s), kg/m^3	< 1400	> 1400
Expansion	Powder cohesive in nature; difficult to fluidize	Solid particles are spoutable; hence expansion is similar to spouted bed
Bed collapse rate	Very poor as deaeration is not fast	Fastest of all groups because of dense or large size of particles
Mixing	Particle mixing as well as heat transfer between a surface and bed are poorer than Group A and B	Solid mixing is relatively poor; high particle momentum and little particle contact minimize agglomeration; gas velocity in dense phase is high, and hence backmixing of dense-phase gas is less
Bubbling/fluidization	As the interparticle forces are greater than the force exerted by fluid, the powder lifts as slug in small-diameter column or channel; hence bubbling is absent or not reported Agglomeration due to excessive electrostatic force Fluidization is generally possible by using agitator or vibrator to break the channels Electrostatic charges removed by using conductive solids or solids with graphite coating or column wall with oxide coating	Bubbles form at 5 cm above the distributor Bubbles of similar size to those of Group B are possible at same bed height and excess gas flow rate; largest bubbles rise slower than interstitial gas, and hence gas enters the bubble base and comes out at the top

1.4 Approach to Model Gas-Solid Flows

Generally two different approaches may be taken to model the gas-solid flows:

Continuum Approach: This approach is also known as Eulerian-Eulerian approach. The gas and the solid are treated as interpenetrating continua. Here the continuity and momentum equations are written for each phase. This approach requires a constitutive equation for the solid phase to relate the solids stress tensor to the velocity field; the fluid phase is typically modeled as Newtonian. The interphase interaction terms often involve empirical relationships for drag, heat transfer and other exchanges (Jakobsen, 2008).

Combined Continuum: Also known as molecular dynamics or Discrete Element Model (DEM). Here the fluid phase is treated as before a Eulerian approach. The solid phase follows the motion of individual particles tracked using Newton's laws, accounting for collision dynamics between particles. This model includes wall forces and the solid-fluid interaction forces. This approach is known as the Lagrangian approach. Other effects such as heat and mass transfer are also taken into consideration with this Eulerian-Lagrangian approach (Li, 2006).

The focus of this work is the comparison of simulations involving gas-solid flows in a fluidized bed the Continuum approach.

1.5 Gas-Solid Flows with Non-spherical Particles

He Tao and Wenqi (2010) developed a DEM method to simulate the corn-shaped particles flow in a hopper. The corn-shaped particle was described by four overlapping spheres. Contact force and gravity force were considered when establishing the model. In addition, the velocity distribution and voidage variance of corn-shaped and spherical particles were investigated. The results showed that the vertical velocity difference between center and side wall and the horizontal velocity of corn-shaped particles were relatively larger than that of spherical particles (He Tao and Wenqui, 2010). Moreover,

Hilton et al. (2009) presented a re- formulation of the pressure-gradient force model, based on a modified pressure correction method, coupled to a discrete element model with non-spherical grains. The drag relations for the coupling were modified to take into account the grain shape and cross-sectional area relative to the local gas flow. They showed that grain shape has a significant effect on the dynamics of the fluidized bed, including increased pressure gradients within the bed and lower fluidization velocities when compared to beds of spherical particles. A model was presented to explain these effects, showing that they are due to both decreased porosity within the bed as well as the relative particle cross-sectional area creating a greater net drag over the bed (Hilton et al., 2009).

For the proposed work, a fundamental goal will be to obtain non-spherical drag models based on numerical work, the drag force will be assumed as a function of several experimental parameters (C_D , Re , Q , g , etc.). Implementation of this relationship will be done in MFIX. In conjunction with the derived correlations drag relationships will also be compared to those shown by Hilton et al. (2009) where prediction of C_D was estimated as a function of sphericity, as shown in Eqn. (1.1). The sphericity (Φ) represents the ratio between the surface area of the volume equivalent sphere and that of the considered particle, the cross-wise sphericity (Φ_{\perp}) is the ratio between the cross-sectional area of the volume equivalent sphere and the projected cross-sectional area of the considered particle and the lengthwise sphericity (Φ_{\parallel}) is the ratio between the cross-sectional area of the volume equivalent sphere and the difference between half the surface area and the mean projected longitudinal cross-sectional area of the considered particle. Finally, the numerical modeling of particulate and fluid flows will be compared to experimental results obtained for non-spherical particles.

$$c_D = \frac{8}{Re} \frac{1}{\sqrt{\Phi_{\parallel}}} + \frac{16}{Re} \frac{1}{\sqrt{\Phi}} + \frac{3}{\sqrt{Re}} \frac{1}{\Phi^{\frac{3}{4}}} + 0.42 10^{0.4(-\log \Phi)^{0.2}} \frac{1}{\Phi_{\perp}} \quad (1.1)$$

Chapter 2: Literature Review

2.1 Eulerian-Eulerian Models

In general, the Eulerian-Eulerian approach is computationally more efficient and therefore can be applied to systems with a larger number of particles than the Eulerian-Lagrangian approach, which is limited to approximately 100,000 particles. However, incorporation of complex particle physics (e.g., cohesion) is a more difficult task with Eulerian-Eulerian models. The impact of cohesion on such a continuum quantity is more difficult to model than its incorporation on a particle-particle level (as is necessary for the Eulerian-Lagrangian approach). The focus of many subsequent Eulerian-Eulerian efforts has been to incorporate improved constitutive relations for the solid phase. A detailed review of these advances for kinetic-theory relations is given in reviews by Campbell (1990) and Goldhirsch (2003). For a thorough review of the associated Eulerian-Eulerian models, the reader is referred to Enwald et al. (1996), Sinclair (1997) and Van Wachem and Almstedt (2003).

2.2 Eulerian-Lagrangian Models

One of the first efforts to develop an Eulerian-Lagrangian fluidized bed simulation was made by Tsuji et al. (1993). This effort used a soft-sphere, discrete particle treatment, similar to what had been developed by Cundall and Strack (1979) combined it with an Eulerian model for the gas flow. This simulation was used to study bubble flow and the results were shown to compare reasonably well with laboratory experiments. Subsequently the soft-sphere method has been used to study a wide variety of systems. Some examples of topics that have been studied using the soft-sphere method include bubble formation (Gera et al., 1998), mixing (Rhodes et al., 2001), binary systems (Limtrakul et al., 2003), and cohesive systems (Mikami et al., 1998, Rhodes and Wang, 2000, Rhodes et al., 2001, Rhodes et al., 2001). A noted drawback of the soft-sphere approach is that the particles are often made artificially soft

in order to keep the simulation stable (Xu and Yu, 1997). Nonetheless, many efforts have shown that the artificially soft nature of particles in soft-sphere models does not affect the overall particle flow (Gera et al., 1998, Mikami et al., 1998, Kawaguchi et al., 1998, Renzo and Maio, 2004).

Studies by Xu and Yu (1997) and Xu et al. (2000) developed a model that utilized a time-stepped algorithm, however, for each particle overlap the simulation was reversed so that the particles “back-up” to point of incipient contact. The repulsive force was still calculated using a soft-sphere model, but the maximum overlap was limited. This “predictor-corrector” method was used to produce realistic fluidized bed snapshots and pressure drop data.

An alternative to the soft-sphere approach is the application of a hard-sphere technique for the simulation of gas-solid systems. This combination was first utilized by Hoomans et al. (1996). In this system, gas-particle interactions are implemented followed by several collisions which are processed one (instantaneous) collision at a time. Some examples of systems that have been studied using this approach include binary systems (Hoomans et al., 2000), bubbling (Ouyang and Li, 1999, Yuu et al., 2000), clustering (Helland et al., 2000, Van Wachem et al., 2001) and high pressure fluidization (Li and Kuipers, 2002), specific applications such as coal combustion (Zhou et al., 2003) and spray granulation (Goldschmidt et al., 2003).

2.3 Non-Spherical Particles Research

In related areas, several researchers have investigated the effect of particle shape on drag. Most of this work consists of the development of formulas to predict the drag coefficient for particles of various shapes in a stationary fluid. Examples include Hartman et al. (1994), Ganser (1993), Haider and Levenspiel (1989), Swamee and Ojha (1991) and Trang-Cong et al. (2003). All of these researchers show a significant influence of particle shape on drag coefficient. The effect of shape on drag and the methods for determining the drag are also given by Clift et al. (1978). Since non-spherical particles have

different drag coefficients, the changes in interaction with the fluid should be significant. Although research has been done on the drag of non-spherical particles, very few experiments have been attempted to document how the particle's shape affects the flow. An exception to this is research that has been done on free-falling non-spherical particles in the atmosphere (Klett, 1995) where a theoretical investigation was made on predicting the orientation of falling non-spherical particles in the atmosphere and the work of Black (1997), comparing the flow behavior of spherical and non-spherical particles in a confined geometry. In Black's (1997) research he completed several different projects in conjunction with his dissertation. One of these projects was measuring particle size, velocity, and concentration in both a coaxial jet flow and a swirling flow through a cylindrical chamber using both spherical and non-spherical particles. His results showed a significant difference in the flow characteristics between the spherical versus non-spherical particles. However, since then the results of his measurements for the non-spherical particles have been shown to be questionable since his measurement techniques permitted serious small particle bias. Additionally, while the data generated by Black (1997) involves non-spherical particles, the flow through the cylindrical chamber introduces swirl which is difficult to model numerically and therefore produces too much uncertainty in the fluid modeling to allow an evaluation of the particle modeling. A review of laser-based particle measuring methods has also been previously completed by Black et al. (1995), including the laser-based instrumentation for particle analysis available at BYU. The review of the literature related to the behavior of non-spherical particle flow in a backward-facing step shows that there is a need for measurements to be made in order to develop and validate existing computer models and provide valuable information regarding the flow behavior of non-spherical particles.

Additionally, there is evidence showing that a turbulent fluid can significantly increase the drag coefficient of particle especially for non-spherical particles. While very little literature is available discussing the effects turbulent fluids have on the drag on particles, Brucato et al. (1998) studied the

effects that turbulence had on the settling velocities of particles versus that in a still fluid. In their experiment they were able to measure the average particle drag coefficients in a turbulent media by means of a suitable residence time technique of the settling velocity exhibited by a cloud of particles. The data they obtained confirmed that free stream turbulence can significantly increase or decrease a particle's drag coefficient when compared with a still fluid without free stream turbulence.

Moreover, Escudie'a et al. (2006) have experimentally investigated shape based segregation in fluidized beds showing particles with the same volume, but different shape, can segregate. Liu and Litster (1991) investigated the effects of non-spherical particles on the properties of spouted beds. Later, Liu et al. (2008) also investigated the effects of particle shape on both pressure drop and minimum fluidization velocity and showed that all of the shapes considered had lower fluidization velocities than for spheres. Combined theoretical and experimental work has been undertaken specifically determining the effects of particle shape on column pressure drop in packed beds (Dolej's and Machac, 1995).

Existing dynamic fluidized bed models in the literature assume spherical particle geometry; nonetheless, in industry particles are hardly ever spherical. Non-spherical simulations with shapes including ellipsoidal, cubic and super-quadric particles, have been applied in industry. The particle shape effect in granular flow was investigated by Cleary (2008), and Fraige et al. (2008). Mixing was investigated by Cleary et al. (1998), were demonstrated that predicting realistic mixing rates was unable to predict with circular particles. Moreover, Cleary and Metcalfe (2002) predicted mixing rates in the correct order with the inclusion of particle shape. Lastly, the effect of particle shape on many other industrial applications is summarized in Cleary (2004, 2009). Nevertheless, particle shape effect in fluidized beds has become an imperative factor computationally.

2.4 Overview of Current Work

Continuum models treat the particles as a continuous phase via a mass and momentum balance for that phase, along with appropriate constitutive equations. For rapid flows, a kinetic-theory analogy (Campbell, 1990, Goldhirsch, 2003) is typically used to develop constitutive relations needed for continuum models. Inherent in the kinetic-theory approach is the assumption that particle-particle interactions are both binary and instantaneous. As mentioned previously, cohesive forces are not inherently instantaneous and therefore the incorporation of cohesive forces into the kinetic theory framework is not straightforward. Unlike continuum models, discrete-particle simulations track particles in the system via the solution of a separate momentum balance for *each* particle. Most existing descriptions for particle cohesion can be applied to discrete-particle models while not conflicting with any assumptions inherent in the simulation.

Discrete-particle simulations provide a straightforward means of incorporating interparticle attraction because cohesive forces can be applied directly to each particle-particle interaction. Discrete-particle simulations are limited by the computational requirements arising from the solution of a separate momentum balance for each particle. Continuum models based on the kinetic theory provide a less computationally demanding means of investigating particulate flows but are restricted by the assumptions implicit in their constitutive relations (e.g. instantaneous, binary contacts).

2.5 Practical Relevance

In the last decades, the experimental and numerical studies of multiphase flows have surprisingly increased especially gas-solid flows. Investigation of this type has abundant applications in energy, chemical processes, among others. Likewise, fluidization has an important technology breakthrough in coal gasification.

2.5.1 Gasification processes

Gasification is a process that converts carbonaceous materials, such as coal, petroleum, biofuel, or biomass, into CO and H₂ (syngas) by reacting the raw material at high temperatures with a controlled amount of oxygen and/or steam. For this purpose a fluidized bed is used.

Fluidized bed gasifiers as shown in Fig. 2.1 are most useful for fuels that form highly corrosive ash that would damage the walls of slagging gasifiers. Biomass fuels generally contain high levels of corrosive ash. Fuel throughput is higher than for fixed bed gasifiers, but not as high as for the entrained flow gasifier. In entrained flow gasifiers as shown in Fig. 2.2 a dry pulverized solid, an atomized liquid fuel or fuel slurry is gasified with oxygen in co-current flow. The gasification reactions take place in a dense cloud of very fine particles. The high temperatures and pressures mean that a higher throughput can be achieved; however thermal efficiency is somewhat lower as the gas must be cooled before it can be cleaned with existing technology. The high temperatures also mean that tar and methane are not present in the product gas; however the oxygen requirement is higher than for the other types of gasifiers.

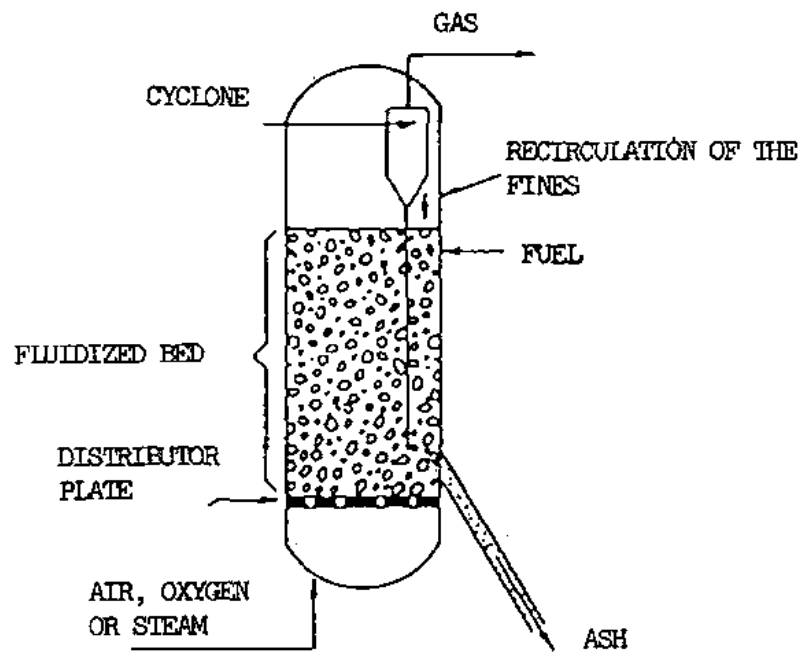


Figure 2.1: Fluidized Bed Gasifier (FAO, 2010)

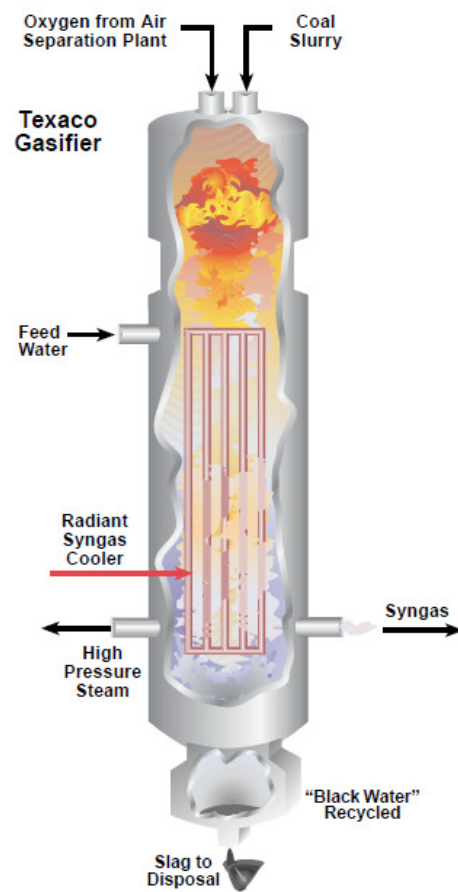


Figure 2.2: Entrained Flow Gasifier (DOE, 2010)

Chapter 3: Objectives

The specific objectives of the proposed work are to:

1. To apply the coupled gas-solid flow capability to the investigation of the detailed physics of fluidized beds. Of particular interest is the investigation of particle size and shape effects.
2. Study the effect of the various drag correlations (published in literature) on the simulation results.
3. To Incorporate Experimental Data for Non-Spherical Particles in MFIX and Fluent, by numerically modeling the minimum fluidization velocities, drag, particle, and fluid flows of non-spherical particles in the fluidized bed.
4. Validate model based on experimental results.

Chapter 4: Fluidization

4.1 Fluidized Bed Behavior

Once the fluid flow rate is increased to produce incipient fluidization, this flow rate value is quoted as a velocity is termed “minimum fluidization velocity”, U_{mf} , defined as

$$U_{mf} = \frac{\dot{V}_{mf}}{A} \quad (4.1)$$

Where \dot{V}_{mf} is the volume flow rate at incipient fluidization and A is the cross-sectional area of the bed containment (Howard, 1989).

Figure 4.1 shows how the pressure drop across the bed changes with respect to the gas velocity.

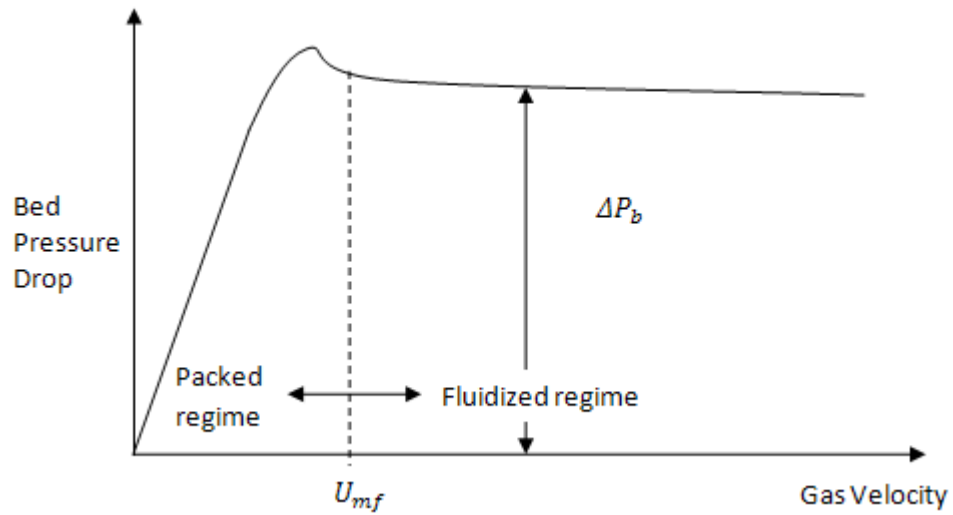


Figure 4.1: Bed Performance with Respect to the Gas Velocity

4.2 Bed Pressure Drop

Once fluidization has been achieved, the pressure drop across the bed, ΔP_b , will be sufficient to support the particle weight, thus

$$\Delta P_b = \frac{M}{\rho_p A} (\rho_p - \rho_f) g \quad (4.2)$$

Where M is the mass of the particles, ρ_p is the particle density, ρ_f is the fluid density, A is the cross-sectional area of the bed containment and g is the gravitational constant (Howard, 1989).

If the density of the fluid is negligible compared to the one of the particles, Equation (4.2) can be simplified to

$$\Delta P_b = \frac{Mg}{A} \quad (4.3)$$

4.3 Flow Modeling

The approach used by Ergun and Orning (1949) modeled a packed bed as a series of identical, straight, parallel channels, and then to form an equation of the form, pressure gradient:

$$\frac{dp}{dx} = av + bv^2 \quad (4.4)$$

Where v is the fluid velocity through the channels and a and b are coefficients. The first and second terms in equation (4.4) are subsequently multiplied by the dimensionless correlation factors α and β , respectively (Howard, 1989).

Thus

$$\frac{dp}{dx} = \alpha av + \beta bv^2 \quad (4.5)$$

Values of α and β were determined by conducting experiments. The coefficient a was obtained from the well known Hagen-Poiseuille equation for Pressure Drop, ΔP_v , over the length, L , of a single straight tube of circular cross section of diameter d , in which the flow is entirely laminar, thus

$$\frac{\Delta P_v}{L} = \frac{32 \mu_f v}{d^2} \quad (4.6)$$

where v is the mean fluid velocity thorough the tube and μ_f is the viscosity.

The pressure drop ΔP_k due to dissipation of kinetic energy in eddies or turbulence will be

$$\frac{\Delta P_k}{L} = \frac{1}{2} \rho_f v^2 \frac{f}{L} \quad (4.7)$$

Where f is a dimensionless friction factor, taken in this case as being equal to L/d .

The total pressure drop ΔP_b over the length L is therefore

$$\frac{\Delta P_b}{L} = 32 \mu_f \frac{v}{d^2} + \frac{1}{2d} \rho_f v^2 \quad (4.8)$$

If the bed is considered to be composed of N such tubes in parallel, then their length L and diameter d can be expressed in terms of the surface area and volume of solid particles in the bed and the bed voidage.

The surface area of the tube walls:

$$A_w = N\pi dL \quad (4.9)$$

And the volume of the fluid in the tubes

$$V_f = \frac{N\pi d^2 L}{4} \quad (4.10)$$

Thus

$$\frac{\text{surface area of tube walls}}{\text{volume of fluid in tubes}}, \frac{A_w}{V_f} = \frac{4}{d} \quad (4.11)$$

If the bed of particles is of depth, containment diameter D and voidage ε then the surface area of particles

$$= \sum(n_p s_p) \quad (4.12)$$

Where n_p and s_p are the number and surface area of particles of each size, p , in the bed, the volume of solid particles

$$= \sum(n_p v_p) = (1 - \varepsilon) \frac{\pi}{4} D^2 L \quad (4.13)$$

Where v_p is the volume of each particle of each size and the volume of voids

$$= \varepsilon \frac{\pi}{4} D^2 L \quad (4.14)$$

Now the surface-to-void volume of the bed, S_{vv} , is to be the same as that of the cluster of tubes,

$$= 4 \sum (n_p v_p) (\varepsilon \pi D^2 L)^{-1} = \frac{4}{d} \quad (4.15)$$

However, from eqn. (4.11)

$$\pi D^2 L = (4 \sum (n_p v_p)) (1 - \varepsilon)^{-1} \quad (4.16)$$

Inserting this into eqn. (4.13) gives

$$d = \left(\frac{4\varepsilon}{1-\varepsilon} \right) / (\text{surface: volume ratio } S_v \text{ of the particles}) \quad (4.17)$$

$$= \left(\frac{4\varepsilon}{1-\varepsilon} \right) \frac{1}{S_v} \quad (4.18)$$

Now the fluid velocity v , through the voids, is related to a superficial fluidizing velocity U by

$$v = \frac{U}{\varepsilon} \quad (4.19)$$

Substituting for v and d in eqn. (4.8) leads

$$\frac{\Delta P_b}{L} = \frac{2(1-\varepsilon)^2}{\varepsilon^2} \mu_f S_v^2 U + \frac{1}{8} \frac{(1-\varepsilon)}{\varepsilon^3} \rho_f S_v U^2 \quad (4.20)$$

Inserting the dimensionless correlation factors α and β gives

$$\frac{\Delta P_b}{L} = 2\alpha \frac{(1-\varepsilon)^2}{\varepsilon^2} \mu_f S_v^2 U + \frac{\beta}{8} \frac{(1-\varepsilon)}{\varepsilon^3} \rho_f S_v U^2 \quad (4.21)$$

Ergun (1952) took the matter further; pointing out that it is customary to use a particle mean size d_m in pressure drop calculations. For spherical particles

$$d_m = \frac{6}{S_v} \quad (4.22)$$

Substitution of this into eqn. (4.21) gives

$$\frac{\Delta P_b}{L} = 72\alpha \frac{(1-\varepsilon)^2}{\varepsilon^2} \frac{\mu_f U}{d_m^2} + \frac{3\beta}{4} \frac{(1-\varepsilon)}{\varepsilon^3} \rho_f \frac{U^2}{d_m} \quad (4.23)$$

(If particles are non-spherical and are of sphericity ϕ and mean size d then d_m is replaced by the product ϕd .)

Dividing each side of the eqn. (3.23) by $(1 - \varepsilon)^2 \mu_f U / \varepsilon^3 d_m^2$ gives

$$\frac{\Delta P_b \varepsilon^3 d_m^2}{L \mu_f U (1 - \varepsilon)^2} = 72\alpha + \frac{3\beta}{4} \frac{1}{(1 - \varepsilon)} \frac{\rho_f U d_m}{\mu_f} \quad (4.24)$$

Where $\rho_f U d_m / \mu_f$ is the particle Reynolds Number Re_p .

Ergun plotted a large amount of data from experiments with different types and sizes of particle and different fluids using equation (4.24). The values of 72α and $3\beta/4$ were found to be 150 and 1.75 respectively. Therefore equation (4.24) is rearranged in the following fashion also for non-spherical particles of sphericity ϕ :

$$\frac{\Delta P_b}{L} = 150 \frac{(1 - \varepsilon)^2}{\varepsilon^3} \frac{\mu_f U}{(\phi d_m)^2} + 1.75 \frac{(1 - \varepsilon)}{\varepsilon^3} \frac{\rho_f U^2}{\phi d_m} \quad (4.25)$$

Eqn. (4.25) is commonly known as the ‘‘Ergun equation’’. The first term of the equation is linear in U and this is dominant when the flow in the voids is laminar. The second term is referred to turbulence (Howard, 1989).

4.4 Theoretical Determination of the Minimum Fluidization Velocity

By equating the Pressure drop across a packed bed, given by the Ergun equation to that of a fluidized bed, and solving for the velocity U , the obtained value will be the minimum fluidization velocity U_{mf} . The previous approach was suggested by Ergun and Orning (1949) (Howard, 1989).

Moreover, substituting $(1 - \varepsilon)(\rho_p - \rho_f)gL$ (where g is the gravitational acceleration) for ΔP_b , ε_{mf} for ε , and U_{mf} for U in equation (3.25) lead to:

$$(1 - \varepsilon)(\rho_p - \rho_f)gL = 150 \frac{(1 - \varepsilon_{mf})^2}{\varepsilon_{mf}^3} \frac{\mu_f U_{mf}}{(\varphi d_m)^2} + 1.75 \frac{(1 - \varepsilon_{mf})}{\varepsilon_{mf}^3} \frac{\rho_f U_{mf}^2}{\varphi d_m} \quad (4.26)$$

Multiplying each side by $\rho_f d_m^3 / \mu_f^2 (1 - \varepsilon_{mf})$ gives

$$\frac{\rho_f (\rho_p - \rho_f) g d_m^3}{\mu_f^2} = 150 \frac{(1 - \varepsilon_{mf})}{\varphi^2 \varepsilon_{mf}^3} \frac{\rho_f U_{mf} d_m}{\mu_f} + \frac{1.75}{\varphi \varepsilon_{mf}^3} \frac{\rho_f^2 U_{mf}^2 d_m^2}{\mu_f^2} \quad (4.27)$$

The left-hand side of eqn. (4.27) is the dimensionless number known as the Archimedes Number, Ar :

$$Ar = \frac{\rho_f (\rho_p - \rho_f) g d_m^3}{\mu_f^2} \quad (4.28)$$

On the right-hand side of Eqn. (4.27) appears the Reynolds Number based on the minimum fluidization velocity and particle diameter. Thus:

$$Ar = 150 \frac{(1 - \varepsilon_{mf})}{\varphi^2 \varepsilon_{mf}^3} Re_{mf} + \frac{1.75}{\varphi \varepsilon_{mf}^3} Re_{mf}^2 \quad (4.29)$$

Furthermore, Wen and Yu were the first to use this type of correlation and to solve it for Re_{mf} . In order to arrive at a suitable solution, Wen and Yu collected the data for ε_{mf} and φ_s and the following approximations were found:

$$\frac{(1-\varepsilon_{mf})}{\varphi^2 \varepsilon_{mf}^3} \cong 11 \text{ and } \frac{1.75}{\varphi \varepsilon_{mf}^3} \cong 14 \quad (4.30)$$

The Wen and Yu correlation expressed using Re_{mf} and Ar is

$$Ar = 24.5 Re_{mf}^2 + 1650 Re_{mf} \quad (4.31)$$

The solution for Re_{mf} , which has the form given in eqn. (4.29), can be written as:

$$Re_{mf} = ((A_1 + B_1 Ar))^{1/2} - A \quad (4.32)$$

The values of A_1 and B_1 depend on the experimental conditions and the range of Re_{mf} . The values of constants A_1 and B_1 in eqn. (4.32) that satisfy the various correlations reported in the literature by various researchers are presented in Table 2 (Gupta and Sathiyamoorthy, 1999).

Table 2: Basic Form of Correlations for Re_{mf} Derived from Pressure Drop Principles (Gupta and Sathiyamoorthy, 1999)

Correlation: $Re_{mf} = (A_1^2 + B_1 Ar)^{1/2} - A_1$, $\alpha = (1 - \epsilon)/\phi_s^2 \epsilon^3$, $\beta = 1/(\phi_s \epsilon^3)$, $m = \alpha/\beta$				
Ref.	Constants			Remarks
	A_1	B_1	m	
Ergun ⁴²	$42.85/\alpha$	$0.57/\beta$	$(1 - \epsilon)/\phi_s$	Modified for fluidized bed
Wen and Yu ³³	33.7	0.0408	0.7857	Water-fluidized, spherical particle
Bourgeois and Grenier ⁴⁴	25.46	0.0382	0.594	Spherical particle
Ghosal and Mukherjee ⁴⁵	29.2	0.029	0.6814	For spherical and angular ($1 < Re_{mf} < 1000$)
Saxena and Vogel ⁴⁶	25.28	0.0571	0.5899	Air fluidized, $6 < Re_{mf} < 102$
Babu et al. ⁴⁷	25.25	0.0651	0.5892	High pressure (7000 kPa) for coal gasification
Richardson and Jeromino ⁴⁸	25.7	0.0365	0.5997	
Thonglimp et al. ⁴⁹	19.9	0.03196	0.4644	Binary system
Chitester et al. ⁵⁰	28.7	0.0494	0.6697	High-pressure fluidization (6485 kPa)
Thonglimp et al. ³⁰	31.6	0.0925	0.7374	Air fluidized
Masaaki et al. ⁵¹	33.95	0.0465	—	Elevated temperature (280–800 K) and pressure (0.1–4.9 MPa)
Agarwal and O'Neil ⁵²	42.81	0.061	0.999	—
Satyanarayana and Rao ⁵³	30.10	0.0417	0.7024	Elevated temperature (295–490 K)
Grace ⁵⁴	27.2	0.0408	0.635	Correlation from literature
Panigrahi and Murty ⁵⁵	32.2	0.0382	0.751	Trial-and-error method adopted to develop general correlation for spherical multiparticle drag coefficient

Chapter 5: Simulation Phase Models

5.1 Gas-Phase Governing Equations

5.1.1 Volume Fraction Equation

By means of the averaging approach to model equations, new field variables are introduced. These are the phasic volume fractions; they represent the fraction of averaging the volume taking place by various phases. By concept, the volume fractions of all the phases must add to one:

$$\varepsilon_g + \varepsilon_s = 1 \quad (5.1)$$

where ε_g is the volume for the fluid phase, also known as the void fraction, and ε_s , the volume fraction for the solid phase (Syamlal et al., 1993).

5.1.2 Continuity Equation

The fluid phase is modeled by solving an average mass and momentum balance. The continuity equation is given by:

$$\frac{\partial}{\partial t} (\varepsilon_g \rho_g) + \nabla \cdot (\varepsilon_g \rho_g \vec{v}_g) = 0 \quad (5.2)$$

where ε_g is the void fraction, ρ_g is the gas density and \vec{v}_g is the gas velocity. The first term in equation (5.2) represents the increase of mass per unit volume and the second term represents the flux of convective mass per unit volume (Anderson and Jackson, 1967).

5.1.3 Momentum Equation

The balance of momentum is given by

$$\frac{\partial}{\partial t} (\varepsilon_g \rho_g \vec{v}_g) + \nabla \cdot (\varepsilon_g \rho_g \vec{v}_g \vec{v}_g) = \nabla \cdot \vec{S}_g + \varepsilon_g \rho_g \vec{g} - \vec{I}_{gs} \quad (5.3)$$

where the first term on the left-hand side refers to the increase of momentum per unit volume and the second term refers to the rate of momentum gain by convection per unit volume. On the right-hand side,

the first term describes the rate of momentum transfer by normal and shear stress components per unit volume; \overline{S}_g is the gas-phase stress tensor, the second term explains the net gravitational force on the fluid per unit volume; \vec{g} is the acceleration due to gravity, and the last term represents the interaction force between the fluid and solid phases per unit volume; \overline{I}_{gs} is the rate of momentum transfer between the gas and solid phase per unit volume (Syamlal et al., 1993).

The gas-solid momentum transfer is described by:

$$\overline{I}_{gs} = -\varepsilon_s \nabla P_g - F_{gs}(\vec{v}_s - \vec{v}_g) \quad (5.4)$$

where P_g is the gas-phase pressure and \vec{v}_s is the average solids velocity. The drag coefficient F_{gs} is determined by two types of experimental data. One type is available as correlations for the terminal velocity. In fluid dynamics an object is moving at its *terminal velocity* if its speed is constant due to the restraining force exerted by the air, water or other fluid through which it is moving. A free-falling object achieves its terminal velocity when the downward force of gravity (weight) equals the upward force of drag. This causes the net force on the object to be zero, resulting in an acceleration of zero.

5.2 Drag Correlations

5.2.1 Syamlal-O'Brien Correlation

Syamlal and O'Brien derived the following equation for converting terminal velocity correlations to drag correlations (Syamlal and O'Brien, 1989):

$$F_{gs} = \frac{3\varepsilon_s \varepsilon_g \rho_g}{4v_t^2 d_p} C_{D-sphere} |\vec{v}_s - \vec{v}_g| \quad (5.5)$$

where d_p is the particle diameter and v_t is the terminal velocity . The single-sphere drag coefficient $C_{D-sphere}$ is defined by the formula given by Dalla Valle (Dalla Valle, 1948):

$$C_{D-sphere} = \left(0.63 + 4.8 \sqrt{\frac{v_t}{Re}}\right)^2 \quad (5.6)$$

The terminal velocity v_t is described by the following correlation modeled by Garside and Al-Dibouni (Syamlal, 1987):

$$v_t = 0.5 \left(A - 0.06Re + \sqrt{(0.06Re)^2 + 0.12Re(2B - A) + A^2} \right) \quad (5.7)$$

where

$$A = \varepsilon_g^{4.14} \quad (5.8)$$

$$B = \begin{cases} 0.8\varepsilon_g^{1.28} & \varepsilon_g \leq 0.85 \\ \varepsilon_g^{2.65} & \varepsilon_g > 0.85 \end{cases} \quad (5.9)$$

and the Reynolds number, Re is defined as

$$Re = \frac{d_p |\vec{v}_s - \vec{v}_g| \rho_g}{\mu_g} \quad (5.10)$$

where μ_g is the gas viscosity (Richardson and Zaki, 1954).

5.2.2 Gidaspow Correlation

The other type of data available for drag formulation, is valid for high value of solids volume fraction, is packed-bed pressure data expressed in the form of a correlation, such as the Ergun equation. Such a correlation must be complemented with a drag correlation for low values of the solids volume fraction. Such correlation is the Gidaspow drag correlation (Gidaspow et al., 1992):

$$F_{gs} = \begin{cases} \frac{3}{4} C_{D-sphere} \frac{\rho_g \varepsilon_g \varepsilon_s |\vec{v}_s - \vec{v}_g|}{d_p} \varepsilon_g^{-2.65} & \varepsilon_g \geq 0.8 \\ \frac{150 \varepsilon_s (1 - \varepsilon_g) \mu_g}{\varepsilon_g d_p^2} + \frac{1.75 \rho_g \varepsilon_s |\vec{v}_s - \vec{v}_g|}{d_p} & \varepsilon_g < 0.8 \end{cases} \quad (5.11)$$

The single-sphere drag coefficient $C_{D-sphere}$ is defined by the formula

$$C_{D-sphere} = \begin{cases} 24/Re(1 + 0.15Re^{0.687}) & Re \leq 1000 \\ 0.44 & Re > 1000 \end{cases} \quad (5.12)$$

and the Reynolds number, Re is defined as

$$Re = \frac{\varepsilon_g \rho_g |\vec{v}_s - \vec{v}_g| d_p}{\mu_g} \quad (5.13)$$

5.3 Solid-Phase Governing Equations

5.3.1 Continuity Equation

The solid phase is modeled by solving an average mass and momentum balance. The continuity equation is given by:

$$\frac{\partial}{\partial t} (\varepsilon_{sm} \rho_{sm}) + \nabla \cdot (\varepsilon_{sm} \rho_{sm} \vec{v}_{sm}) = 0 \quad (5.14)$$

where ε_{sm} is the m^{th} solids volume fraction, ρ_s is the m^{th} solids density and \vec{v}_s is the m^{th} solids velocity. The first term in equation (5.14) represents the increase of mass per unit volume and the second term represents the flux of convective mass per unit volume (Syamlal, 1987).

5.3.2 Momentum Equation

The balance of momentum is given by

$$\frac{\partial}{\partial t}(\varepsilon_{sm} \rho_{sm} \overrightarrow{v_{sm}}) + \nabla \cdot (\varepsilon_{sm} \rho_{sm} \overrightarrow{v_{sm}} \overrightarrow{v_{sm}}) = \nabla \cdot \overrightarrow{S_{sm}} + \varepsilon_{sm} \rho_{sm} \vec{g} + \overrightarrow{I_{gs}} - \overrightarrow{I_{ml}} \quad (5.15)$$

where the first term on the left-hand side refers to the increase of momentum per unit volume and the second term refers to the rate of momentum gain by convection per unit volume. On the right-hand side, the first term describes the rate of momentum transfer by normal and shear stress components per unit volume; $\overrightarrow{S_{sm}}$ is the m^{th} solids stress tensor, the second term explains the net gravitational force on the solids per unit volume; \vec{g} is the acceleration due to gravity, the next term represents the interaction force between the fluid and m^{th} solid phase per unit volume; $\overrightarrow{I_{gs}}$ is the rate of momentum transfer between the gas and solid phase per unit volume, and the last term $\overrightarrow{I_{ml}}$ is the rate of momentum transfer between the different solid phases per unit volume.

The gas-solid momentum transfer is described by:

$$\overrightarrow{I_{ml}} = F_{ml}(\overrightarrow{v_{sl}} - \overrightarrow{v_{sm}}) \quad (5.16)$$

where $\overrightarrow{v_{sl}}$ is the average solids velocity for the l^{th} solid phase, $\overrightarrow{v_{sm}}$ is the average solids velocity for the m^{th} solid phase. The drag coefficient F_{sl} is represented by a relation derived by Syamlal:

$$F_{ml} = \frac{3(1+e_{lm})(\pi/2+C_{f-lm}\pi^2/8)\varepsilon_{sl}\rho_{sl}\varepsilon_{sm}\rho_{sm}(d_{pl}+d_{pm})^2 g_{o-lm}|\overrightarrow{v_{sl}}-\overrightarrow{v_{sm}}|}{2\pi(\rho_{sl}d_{pl}^3+\rho_{sm}d_{pm}^3)} \quad (5.17)$$

where e_{lm} and C_{f-lm} are the coefficient of restitution and the coefficient of friction, between the l^{th} and m^{th} solid phase particles. The radial distribution function g_{o-lm} is a correction factor that modifies the probability of collisions between grains when the solid granular phase becomes dense. The following equation was derived by Lebowitz for a mixture of hard spheres (Ogawa et al., 1980):

$$g_{o-lm} = \frac{1}{\varepsilon_g} + \frac{3d_{pl}d_{pm}}{\varepsilon_g^2(d_{pl}+d_{pm})} \sum_{n=l}^M \frac{\varepsilon_{sn}}{d_{pn}} \quad (5.18)$$

5.4 Modeling Turbulence: The k - ε model

The k - ε model belongs to the class of *two-equation models*, in which model transport equations are solved for two turbulence quantities-i.e. k and ε in the k - ε model. From these two quantities can be formed a lengthscale ($L = k^{3/2}/\varepsilon$), a timescale ($\tau = k/\varepsilon$), a quantity of dimension $\nu_T(k^2/\varepsilon)$. As a consequence, two-equation models can be complete-flow-dependent specifications such as a mixing length ($l_m(x)$) are not required [20].

The two transport equations are the following:

$$\frac{\bar{D}k}{\bar{D}t} = \nabla \cdot \left(\frac{\nu_T}{\sigma_k} \nabla k \right) + P - \varepsilon \quad (5.19)$$

$$\frac{\bar{D}\varepsilon}{\bar{D}t} = \nabla \cdot \left(\frac{\nu_T}{\sigma_\varepsilon} \nabla \varepsilon \right) + C_{\varepsilon 1} \frac{P\varepsilon}{k} - C_{\varepsilon 2} \frac{\varepsilon^2}{k} \quad (5.20)$$

Where k is the turbulent kinetic energy, ε turbulent dissipation rate, P is the turbulence production, ν_T is the turbulent viscosity, and σ_k the turbulent Prandtl number.

The standard values of all model constants are

$$C_\mu=0.09, \quad C_{\varepsilon 1}=1.44, \quad C_{\varepsilon 2}=1.92, \quad \sigma_k=1.0, \quad \sigma_\varepsilon=1.3 \quad (5.21)$$

Chapter 6: Fluidized Bed Simulation

The work done in this research was divided in to two parts. The first part corresponds to the investigation of fluidized bed with spherical particles. The second part involves the investigation of fluidization with non-spherical particles. To simplify the complexities involved in obtaining the solution of the modeling equations, the following assumptions were made:

- a) The fluid simulation domain was assumed to be centered at the bottom of the vessel containing the particles.
- b) An Eulerian-Eulerian approach for both the fluid and the solid phase was considered for the simulation.

For the first study two spherical drag correlations were compared to the Ergun equation and experimental data for validation of the numerical model. The theoretical correlations employed in order to predict and compare fluidization conditions with spherical particles were:

1. Syamlal and O'Brien drag correlation, according to Equation (5.5).
2. Gidaspow drag correlation, according to Equation (5.11).

For the investigation of non-spherical particles, the work is divided in to three sections:

1. The implementation of a non-spherical drag correlation found in literature, as presented in Hölzer and Sommerfeld (Hölzer and Sommerfeld, 2008).
2. The calculation of drag coefficient of a solid non-spherical particle moving at the terminal velocity is being studied. The numerical approximations are done using the solver FLUENT on a collocated grid. The non-spherical particle shape simulated in this study was elliptical. Experimental drag results are compared to experimental data for validation.
3. The derivation of a simple correlation formula for the standard drag coefficient of arbitrary shaped particles using a large number of experimental data specifically recorded for this work. This new correlation formula accounts for the particles sphericity (shape coefficient) over an

entire range of Reynolds numbers up to the critical Reynolds number. Such a correlation was used for CFD fluidized hydrodynamic modeling in uniform flow.

6.1 Spherical Particles Modeling

The experimental test bed consists of:

- 1mm (d_p) spherical particles.

The particles are made of Borosilicate glass which is widely used for laboratory glassware. Table 3 shows the physical properties of Borosilicate glass. The particles are contained in a cylindrical vessel of specific diameter and height. For the computational analysis only a portion of the vessel height is considered since the actual height of the vessel is larger compared to that of the bed. In addition, a static bed height was determined in order to perform the investigation. As shown in Fig. 6.1-a). The fluid simulation domain consists of a two-dimensional rectangular system (12 cm x 50 cm) with the origin of the x -, y - axis centered at the left bottom corner of the rectangle.

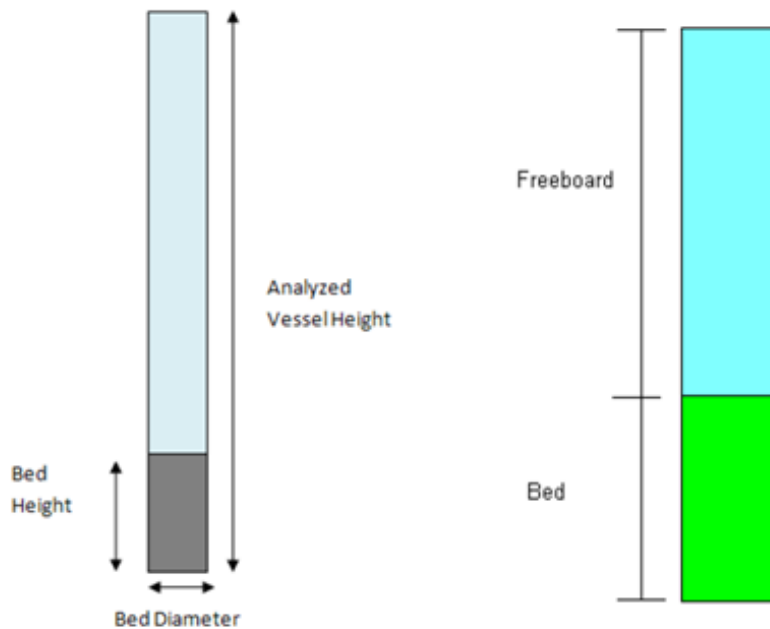


Figure 6.1: a) Particle Bed Setup b) MFI analysis sections

For this investigation, a set of computational grids are generated in both FLUENT and MFIX in order to achieve particular grid independence. The first computational grid was a coarse mesh with 1200 cells. Next grid was 4800 cells, the third 24200 cells, another 64400 cells and a last of 100625 cells. By checking the pressure values it was observed that after the 64400 cell-grid the results were within a 2% deviation; however the computational time increases as the number of cells increases. Thus, a last computational grid was generated but now containing a finer mesh only in the particle bed region, and axially growing coarser by a factor of 0.2, this grid was 35420 cells. The working fluid is air at isothermal condition. The fluid properties are obtained at 25 °C, with density of 1.2 kg/m³, dynamic viscosity of 1.8e⁻⁰⁵ Pa-s. The particles bed has an initial height of 5.5 cm; this bed height was utilized for all the simulations and validation performed in this paper. For MFIX, the bed was divided into a bed section and a freeboard section with the former taking up the bottom half of the bed space, as shown in Fig. 6.1-b). For MFIX, the gas void fraction was set to a typical value at minimum fluidization. The gas velocity is initially set in the y-direction. In the freeboard section the void fraction is initially set to unity and the y-component of the gas velocity is initially set to value higher than the one attained at inlet velocity (typically a factor of 4 is accurate).

Table 3: Borosilicate glass physical properties (Vogel, 1994)

Physical Properties	
SiO ₂ = 80.6%	Coefficient of expansion (20°C–300°C) 3.3 x 10 ⁻⁶ K ⁻¹
B ₂ O ₃ = 13.0%	Density 2.23g/cm ³
Na ₂ O = 4.0%	Refractive index (Sodium D line) 1.474
Al ₂ O ₃ = 2.3%	Dielectric constant (1MHz, 20°C) 4.6
Optical Information	Specific heat (20°C) 750J/kg°C

The values for the initial and boundary conditions for both bed and freeboard sections are shown in Table 4. In order to produce fluidization curves, most simulations were run with inlet conditions that

varied with time. For the initial conditions in FLUENT, the bed is divided into a “bed” region and a “freeboard” region with the former taking up the bottom half of the bed and the latter comprising the top half. In the bed region, the solids void fraction is initially set to 0.63, since Fluent handles solids volume fraction instead of gas volume fraction as MFIX. The gas velocity is initially set to 5 cm/s in the axial direction. The boundary conditions for the gas phase consist of no-slip, impermeable walls on the vertical sides of the bed. For the outflow boundary condition at the top of the bed, a Pressure Outlet set at atmospheric pressure (101325 Pa) is specified across the entire width. At the bed inlet, a velocity inlet boundary condition is specified.

Table 4: MFIX simulation parameters

MFIX initial conditions		MFIX boundary conditions	
Bed Section		Pressure Outlet	101325 Pa
Gas Void Fraction (ε_g)	0.37	Walls	No-slip
		Velocity Inlet	5-130 cm/s
Gas Velocity (v_g)	5 cm/s	Inlet Gas Void Fraction (ε_g)	1.0
Freeboard Section			
Gas Void Fraction (ε_g)	1.0		
Gas Velocity (v_g)	40 cm/s		

6.2 Non-Spherical Particles Modeling

6.2.1 Literature Non-Spherical Drag Correlation

The non-spherical correlation implemented into FLUENT and MFIX depends on the shape and orientation, for the sake of this analysis the equation was modified to only take into account the shape of particles:

$$C_{D-non_spherical} = \frac{24}{Re} \frac{1}{\sqrt{\phi}} + \frac{3}{\sqrt{Re}} \frac{1}{\phi^{3/4}} + 0.421 \times 10^{0.4(-\log \phi)^{0.2}} \frac{1}{\phi} \quad (6.1)$$

The sphericity ϕ represents the ratio between the actual particle volume and that of the equivalent sphere. In order to characterize the non-spherical particles for comparison to spherical particles the sphericity was used. The sphericity was calculated using the expressions shown below (Boggs, 1967):

$$\phi = \sqrt[3]{\frac{\text{Particle Volume}}{\text{Circumscribed Sphere Volume}}} \quad (6.2)$$

In order to calculate the sphericity of a particle, a tri-axial ellipsoid having three diameters was imposed on the surface of the particle being investigated. An example of the three lengths used for a non-spherical particle in this study is shown in Fig. 6.2. Substitution of these lengths into Eqn. (11), results in the following:

$$\phi = \sqrt[3]{\frac{bc}{a^2}} \quad (6.3)$$

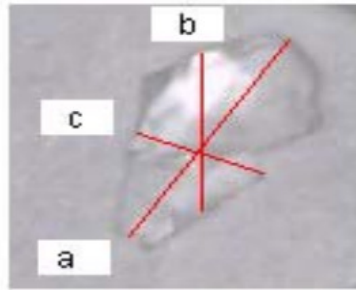


Figure 6.2: Actual photograph showing sphericity analysis of a non-spherical particle

The non-spherical particles have the following parameters:

- 0.85 mm (d_m) and sphericity of 0.55 non-spherical particles.

Furthermore, the CFD modeling is carried out in the exact same way as for spherical particles (same Initial and Boundary Conditions), although for the non-spherical analysis a modification to the codes (FLUENT and MFIX) was made in order to take into account the non-spherical drag correlation. Both codes only deal with drag correlations designed for spherical particles. Thus a sub-routine written in C++ language was implemented into the Codes. By using Eqn. (5.5), the Syamlal-O'Brien drag correlation as baseline, the drag coefficient was changed from that of Eqn (5.6), Dalla Valle to the one of Eqn. (6.1), the Hölzer and Sommerfeld equation. The non-spherical drag correlation sub-routine is described in the Appendix.

6.2.2 Single Non-Spherical Particle Drag Analysis

For the numerical simulation a rice grain was modeled. The shape was approximated as that of an ellipsoid as shown in Figure 6.3. The following semi-axis parameters were set to be the same as the rice grain used in the experimental portion of the results where $a = 3.38$ mm, $b = 1.04$ mm and $c = 0.86$ mm. The rice grain density (ρ_s) was determined to be 577 kg/m^3 , and particle mass (m_s) was determined to be 2.33 mg using a high accuracy digital mass scale.

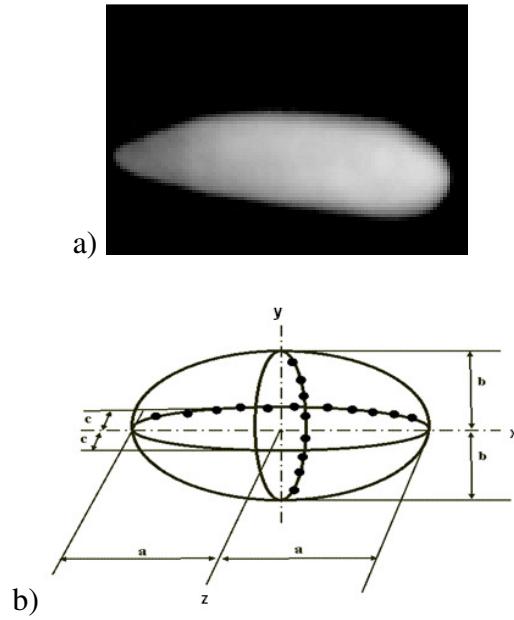


Figure 6.3: Non-spherical geometric approximation: a) particle used, b) ellipsoid

In order to calculate the terminal velocity of the particle an analysis was performed on the non-spherical particle. The particle was assumed to fall under the influence of gravity with other forces acting on the particle including buoyancy and drag. A force balance results in:

$$W = F_b + D \quad (6.4)$$

For the ellipsoidal shape:

$$W = m_s g = \frac{4}{3} \pi abc \rho_s g \quad (6.5)$$

$$F_b = \frac{4}{3} \pi abc \rho_f g \quad (6.6)$$

$$D = C_D \frac{1}{2} \rho_f v_s^2 A \quad (6.7)$$

Where $g = 9.81 \text{ m/s}^2$, ρ_s = density of the fluid (air) = 1.22 kg/m^3 , $A = \pi ac$, and was initially assumed as $C_D = 0.6$ which is the drag force acting on the surface of an elliptical cylinder at comparable Reynolds numbers.

Substitution of Eqns. (6.5-7) in Eqn. (6.4) and solving for the terminal velocity, v_t , yields the following expression:

$$v_t = \sqrt{\frac{8 \text{ bg } (\rho_s - \rho_f)}{3 C_D \rho_f}} \quad (6.8)$$

The value of v_t with these assumptions was initially determined to be 4.6 m/s. This provided a starting value of the velocity needed for the test to be performed. The terminal velocity was later determined during the simulation.

The particle velocity was used to calculate a Reynolds number based on the largest semi-axis length of the ellipsoid in this case a , where the viscosity of the fluid μ_f is taken to be 1.8×10^{-5} kg/m-s:

$$\text{Re} = \frac{\rho_f v_s a}{\mu_f} \quad (6.9)$$

The particle drag coefficient was also calculated with the following equation:

$$C_D = \frac{F}{\frac{1}{2} \rho_f v_s^2 A} \quad (6.10)$$

a) Numerical Modeling

The numerical approximations were achieved using the solver FLUENT. The parameters defined in the previous section were used in the software for the model. The model was analyzed assuming the non-spherical element was set to move downwards at free-falling conditions, and a moving mesh was used. In order to test possible moving mesh methods, several grid configurations were used for the analysis. The assumption used for all the simulations was a two-dimensional domain. The boundary conditions and mesh dimensions are labeled in Figure 6.4. A moving wall condition is assigned to boundary 1 and a no-slip wall condition assigned to boundary 4 while a pressure-outlet condition was set for boundaries 2,3 and 5.

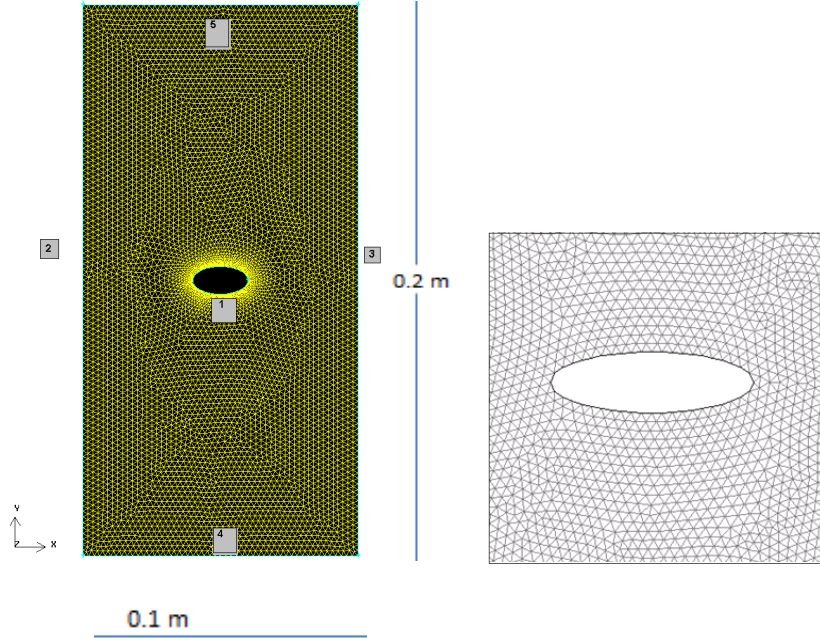


Figure 6.4: Grid domain and boundary conditions

For the moving mesh analysis additional parameters were calculated. The translation and possible rotation of the non-spherical particle, the degrees of freedom, and the deformation of the elements were done using a User Defined Function (UDF). The parameters concerning the particle are considered including: the mass of the particle and the mass-moments of inertia.

The following equations present the mass moment of inertia calculations about three axes:

$$I_{zz} = m_s \frac{(a^2+b^2)}{5} = 5.818 \times 10^{-12} \text{ kg-m}^2 \quad (6.11)$$

$$I_{yy} = m_s \frac{(c^2+a^2)}{5} = 5.66 \times 10^{-12} \text{ kg-m}^2 \quad (6.12)$$

$$I_{xx} = m_s \frac{(b^2+c^2)}{5} = 8.47 \times 10^{-13} \text{ kg-m}^2 \quad (6.13)$$

The first moving mesh was then tested, and the particle was simulated to fall for 10 ms with a time step of 0.01 ms, for this grid the elements around the particle were also deforming and output non-constant values for the elements surrounding the particle. Thus, the first mesh was not used. For next tested mesh modifications were made and a constant-size region of elements surrounding the particle was created. The chosen elements for this region were quadrilateral elements, as shown in Figure 6.5. Some uneven distortion was still appreciated in the triangular elements surrounding the quad-element particle region, especially in the corners, since it is a rectangular region.

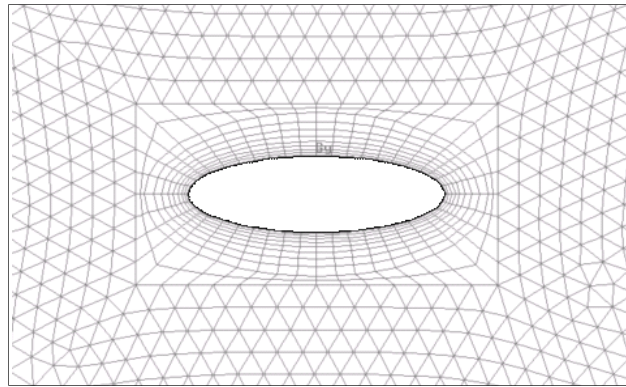


Figure 6.5: Grid with particle rectangular-constant-size quad elements region

The third grid was modified to have an elliptical constant element-size region surrounding the particle, as shown in Figure 6.6, with this change a more reliable element distortion and remeshing was achieved. For this reason this grid was chosen for the moving mesh analysis.

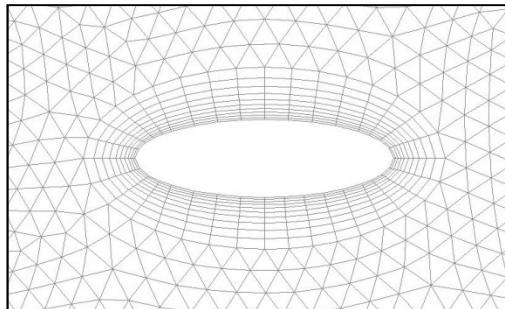


Figure 6.6: Grid with particle elliptical-constant-size quad elements region

6.2.3 Experimental Non-Spherical Drag Correlation

In this section, an experimental investigation is performed in order to develop a correlation of drag coefficient as a function of Reynolds number for non-spherical particles of a specific sphericity. In addition this drag correlation is implemented in a computational model for gas-solid fluidized bed with non-spherical particles in uniform flow.

This study was based on the general drag correlation proposed by Haider and Levenspiel (Haider and Levenspiel, 1989), all of which happen to contain 4 arbitrary constants, as described in Eqn. (6.14):

$$C_D = \frac{24}{Re} (1 + A Re^B) + \frac{C}{1 + \frac{D}{Re}} \quad (6.14)$$

This drag correlation is used in order to fit the non-spherical experimental data specifically recorded for this work. A non-linear least squares numerical technique is performed and in conjunction with a Newton-Raphson iterative scheme and the following equation was developed fitting the non-spherical experimental data.

The non-spherical particles have the following parameters:

- 1.15 mm (d_m) and sphericity of 0.55 non-spherical particles.

Furthermore, the CFD modeling is carried out in the exact same way as for spherical particles (same Initial and Boundary Conditions), although for the non-spherical analysis a modification to the codes (FLUENT and MFX) was made in order to take into account the non-spherical drag correlation. Both codes only deal with drag correlations designed for spherical particles. Thus a sub-routine written in C++ language was implemented into the Codes. By using Eqn. (5.5), the Syamlal-O'Brien drag correlation as baseline, the drag coefficient was changed from that of Eqn (5.6), Dalla Valle to the one

numerically found through the fit given by Eqn. (6.14). The non-spherical drag correlation sub-routine is described in the Appendix.

6.3 Theoretical Correlation Validation

By using the theoretical correlation found in Equation (4.29), based on the pressure drop principles, the minimum fluidization was calculated and compared with those found on the simulations, the equation commonly known as the “Ergun equation”. Also, the predictive results using the Ergun equation are presented alongside the numerical results obtained when using the other drag models.

Chapter 7: Experimental Setup

7.1 Spherical and Non-Spherical Particles

The following setup description was used for all the experimental validation involving fluidized bed behavior, including both spherical and non-spherical particles. The setup is composed of 2 primary sections: a column section and a fluid delivery section (Fig. 7.1). The lower portion of the column section is made of Plexiglas with 12.7 cm outer diameter and 0.318 cm wall thickness. At the bottom portion the Plexiglas section a flow straightener made of ABS plastic is used to uniform distribution of air through the test section. Immediately above this section a mesh catch with 0.053 mm of nominal diameter is used to ensure that the particles remain in the test section. A quartz tube with 12 cm outer diameter and 0.5 cm wall thickness is inserted into the Plexiglas portion and extends up 2m. 1 mm spherical borosilicate glass beads are placed at a height of 5.5 cm in the test section and are assumed to have a sphericity of 1.

To measure pressure drop across the test bed a digital display manometer (Omega HHP4252 with 7 Pa resolution) is used. The fluid delivery section uses Grainger 3.7 kW high-pressure blower to supply air to the test section of packed bed column, a wafer type butterfly valve with 12.7 cm diameter and 1 cm thick flange is used. The butterfly valve is made of cast iron and rated for the pressures and temperatures appropriate to this experiment. Volumetric flow rate is measured using an insertion type thermal mass flow meter with 200 ms response time.

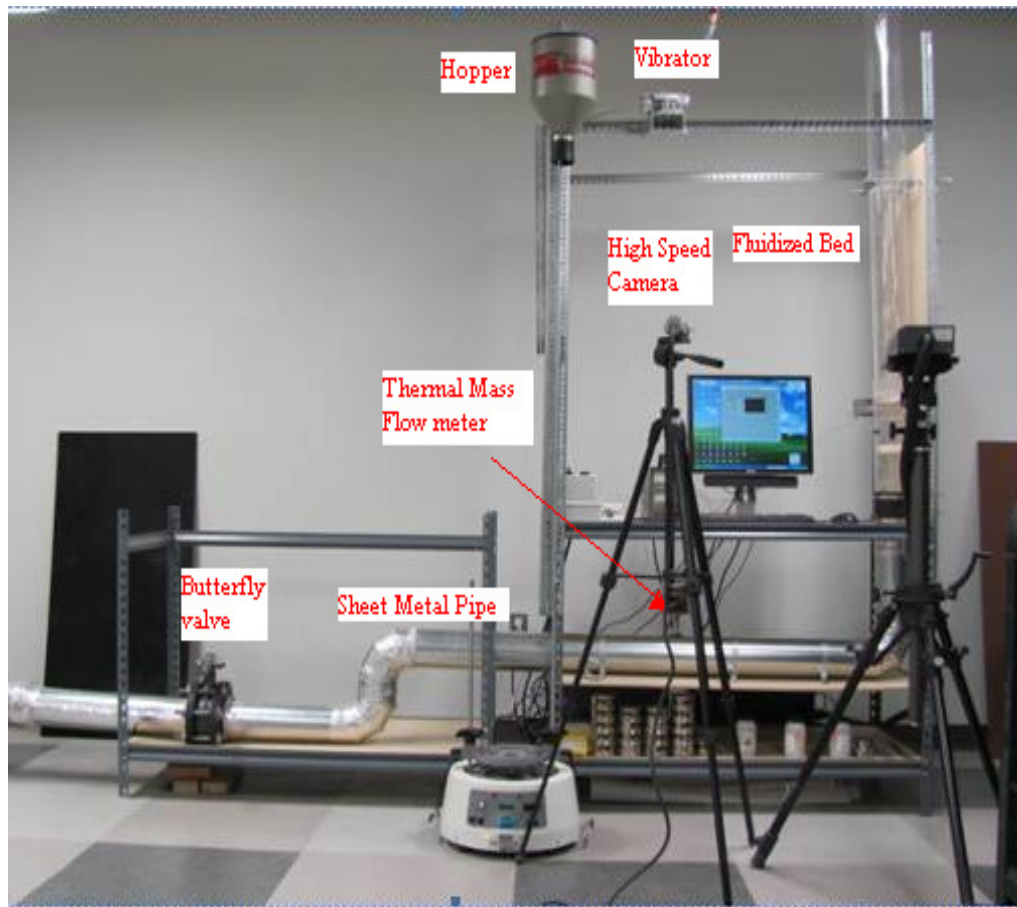


Figure 7.1: Fluidized bed experimental setup

A high-speed camera system, maximum frame of 20,000 frames per second, was used to record particle movement at the base and near the top the fluidized bed. Imaging was acquired at (a) minimum fluidization, (b) transition, and (c) terminal velocity. An example of the particle imaging captured at large (entire bed) and small (individual particles) scales is presented in Fig. 7.2-a). At the terminal velocity condition the camera position on the column was determined based on the maximum height attained (in average) by the particles when lifted by the compressed air.

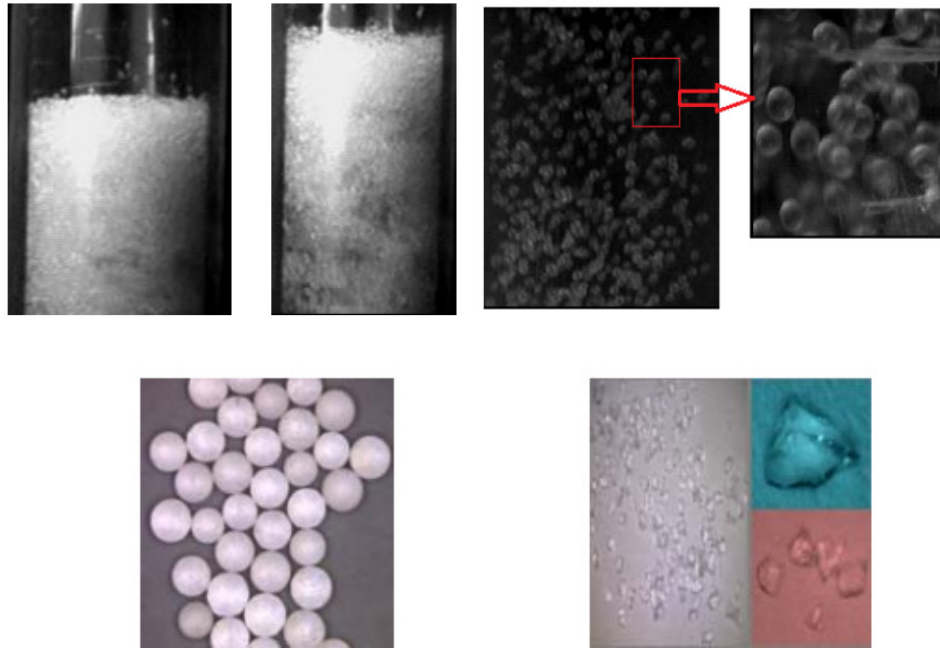


Figure 7.2: a) High-speed particle motion b) Magnified photographs of spherical particles, and non-spherical particles

Moreover, the particle size characterization technique was performed in the following way. Spherical particles assumed sphericity value of 1.0. The non-spherical particles were obtained by crushing 6 mm borosilicate glass beads using a compression machine. Figure 7.2-b) shows a magnified image of both the spherical particles and non-spherical particles captured using a video camera. After crushing beads into the non-spherical particles, a sieve test technique was done to separate the particles by size. Taking the images obtained of the particles a sphericity analysis was performed for a number of individual particles using Eqn. (6.3). The particle sphericity was found in the range of 0.50 to 0.60. Thus, the average 0.55 was considered for the numerical analysis. An individual particle with 0.55 sphericity value was presented in Fig. 6.2 which showed the three diameters (intercepts) of a, b and c. Results showed that the non-spherical particles used in this experiment ranged from 0.9 to 2.0 mm with mean particle size of 1.5 mm.

7.2 Single Non-Spherical Particle Analysis and Non-Spherical Drag Correlation

The following procedure was used in order to predict drag coefficient for non-spherical particles. Both the single particle and the non-spherical drag correlation followed the same methodology for finding drag and Reynolds number data. In addition, the same high-speed camera system as previously described was used capable of recording up to 500 kHz, it captured the particle motion in the free falling stream as shown in Figure 7.3. A single particle motion was captured at a height of 2.2 m from the top of the bed at a rate of 3100 frames per second. A digital image analyzing software Phantom was used to track the particle motion frame by frame from the videos obtained by the high speed camera. The software was used to track the starting and ending point of the free falling particle in the camera frame, and also to track the time required to travel that distance by a single particle. Figure 7.4 shows the motion captured for a falling particle at terminal velocity at 4 intervals of time.

The particle terminal velocity was obtained using Eq. (7.1):

$$V_s = \frac{\Delta S}{\Delta t} \quad (7.1)$$

Where Δs is the distance travelled and Δt is the time required.

Finally, the experimental drag coefficient for a single rice grain was calculated using Eqn. (6.8) and solving for C_D :

$$C_D = \frac{\frac{8}{3} b g (\rho_s - \rho_f)}{\rho_f v_s^2} \quad (7.2)$$

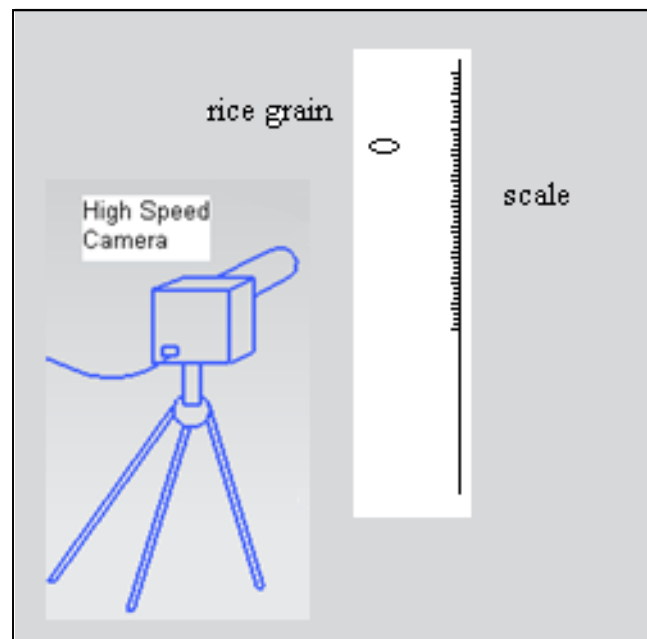


Figure 7.3: Experimental setup

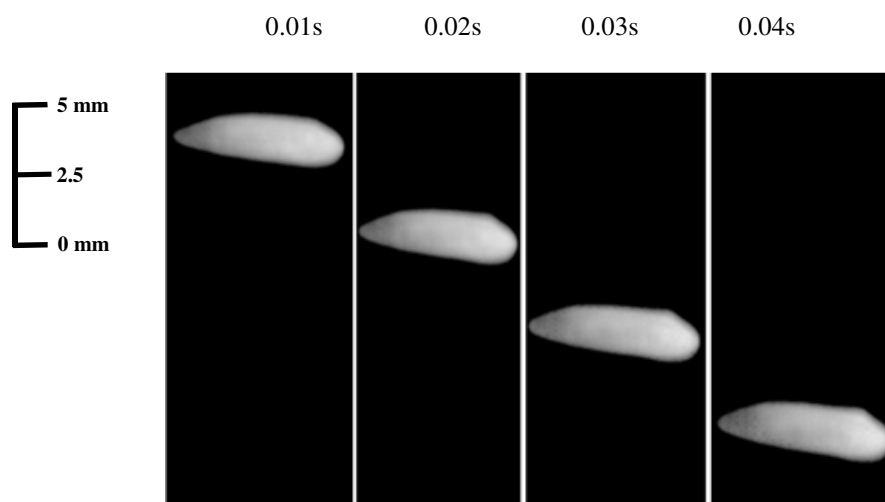


Figure 7.4: Particle motion captured with high-speed camera

Chapter 8: Results and Discussion

8.1 Spherical Particles

Bubbling behavior in the fluidized bed takes place in a transitory way, where splitting and collapsing of bubbles occur, due to this, fluctuations in the pressure drop are anticipated. In line to this, area-weighted average values of pressure drop values are recorded providing a comparison between simulation results. Consequently, time-averaging was carried out over a range of 1–10 seconds of time computation. The first set of simulations was performed using FLUENT with spherical particles, the pressure drop variation inside the bed as the superficial gas velocity increases using the Syamlal-O'Brien and Gidaspow drag models is shown in Fig. 8.1, where numerical values are compared with the experimental and theoretical findings. The plot describes a typical fluidized bed behavior. Where a linear increase of pressure with respect to superficial velocity is seen, also known as packed-bed behavior, until the inflow gas velocity reaches what is known as the minimum fluidization velocity U_{mf} , also the pressure drop reaches a maximum pressure drop value, theoretically this maximum pressure drop value should be equal to the weight of the bed per cross-sectional area of the vessel containing the particles.

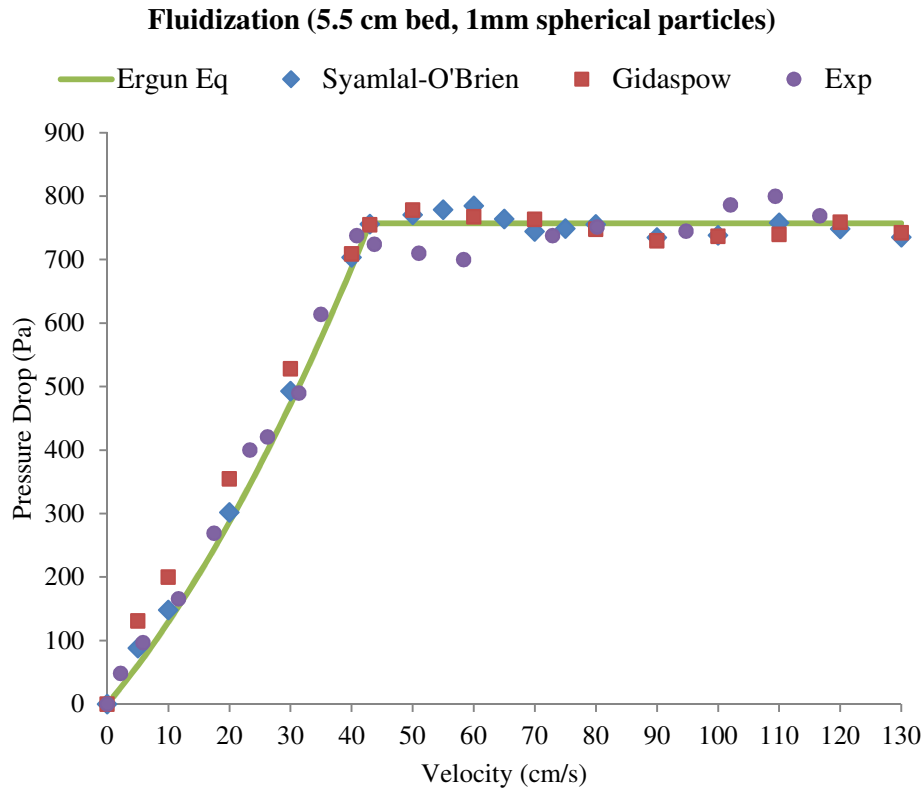


Figure 8.1: FLUENT spherical particles validation with experimental results

Additionally, this pressure drop value remains near continuous showing a relative linear trend with increasing gas velocity once the fluidization point has been reached. As appreciated in Fig. 8.2, MFIX drag models describe with good accuracy the packed-bed behavior with respect to the theoretical and experimental results as well, where a linear increase of pressure with respect to superficial velocity is appreciated, reaching later on the minimum fluidization velocity. In addition, this pressure drop value remains nearby constant showing a comparative linear development with increasing gas velocity, as seen before with the FLUENT results. By further increasing the inflow velocity the established constant pressure drop starts to fluctuate, due to the constant bubbling behavior of the bed. At this instance, FLUENT and MFIX numerical results describe somewhat higher values than the experimental results for both drag models.

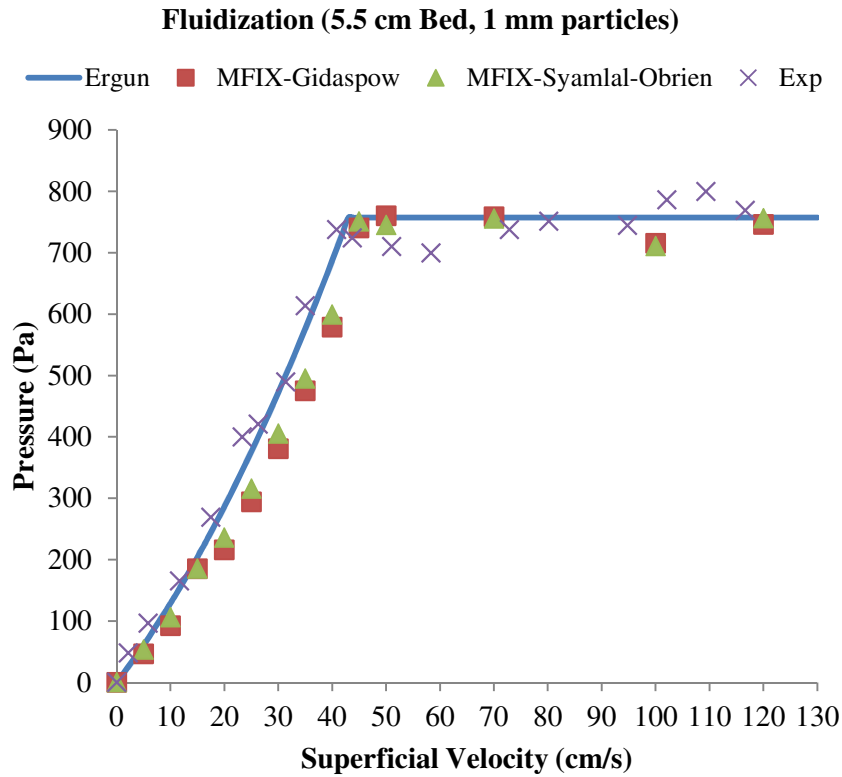


Figure 8.2: MFIx spherical particles validation with experimental results

The validation of the model with spherical particles was done in several steps. The numerical codes were tested for numerical convergence. The methods were stable and converged with the set time step size. The fluid-particle interaction was compared with empirical solutions and experimental observations. Table 5 demonstrates the very good agreement of the measured pressure drop through a fluidized bed (at packed conditions no particle movement is observed since the flow speed is below the minimum fluidization velocity) with the predictions of Ergun's empirical equation and the experimental findings for spherical particles.

Table 5: Numerical, theoretical and experimental results for spherical particles

FLUENT		
Drag Correlation	Min. Fluidization Velocity (cm/s)	Pressure Drop (Pa)
Syamlal-O'Brien	43	755.7
Gidaspow	43	754.6
MFX		
Drag Correlation	Min. Fluidization Velocity (cm/s)	Pressure Drop (Pa)
Syamlal-O'Brien	43	755.0
Gidaspow	43	753.2
THEORETICAL		
Correlation	Min. Fluidization Velocity (cm/s)	Pressure Drop (Pa)
Ergun	43	757.0
EXPERIMENTAL		
Min. Fluidization Velocity (cm/s)	Pressure Drop (Pa)	
43.7	743.0	

In order to provide a more precise understanding about the fluidization hydrodynamics, instantaneous gas and solid flow contours were recorded from within FLUENT and MFX. Flow fields of the axial component of gas velocity at simulated flow time of 1.5 s are given in Fig. 8.3 for spherical particles. Bubbling bed behavior is observed as the flow develops through the gas void between the solid particles, both codes for Syamlal–O'Brien as well as for Gidaspow's drag function show similar behavior. Also, the solid-phase velocity vectors are shown in Fig. 8.4 and a very good agreement between FLUENT and MFX and numerical results is appreciated. In addition, Fig. 8.5 shows the solids volume fraction profile for inflow velocity of 75 cm/s at 1.5 s simulation time, no significant pattern differences exist among the gas volume fraction contours shown in FLUENT and MFX. Numerical results of MFX and Fluent are quite similar for both drag models.

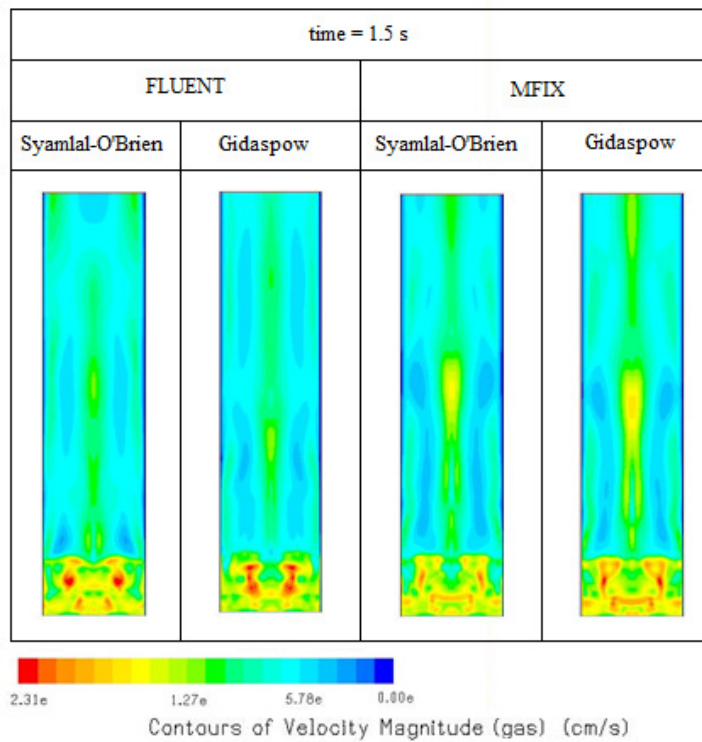


Figure 8.3: Snapshots of gas-axial velocity at 75 cm/s inflow velocity with spherical particles

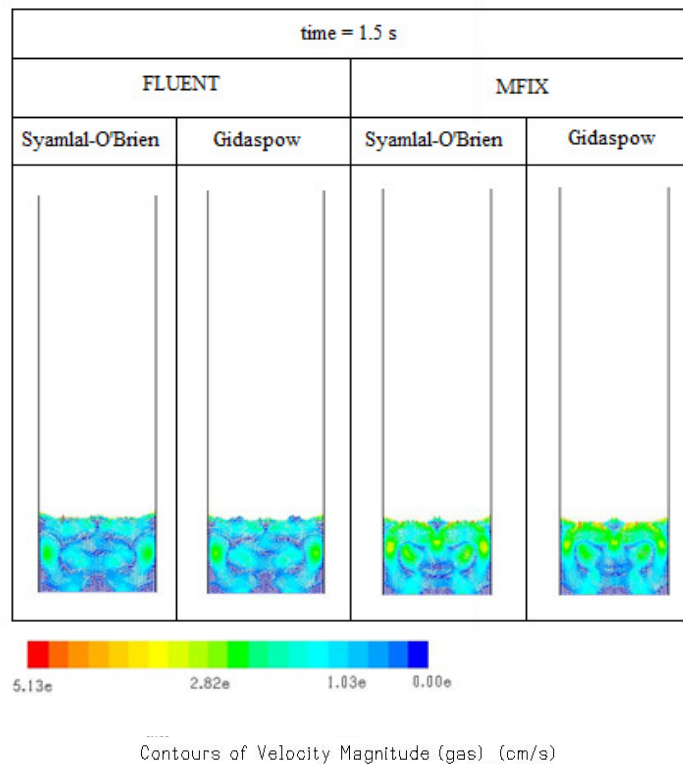


Figure 8.4: Snapshots of solids velocity vector-field for inflow velocity of 75 cm/s with spherical particles

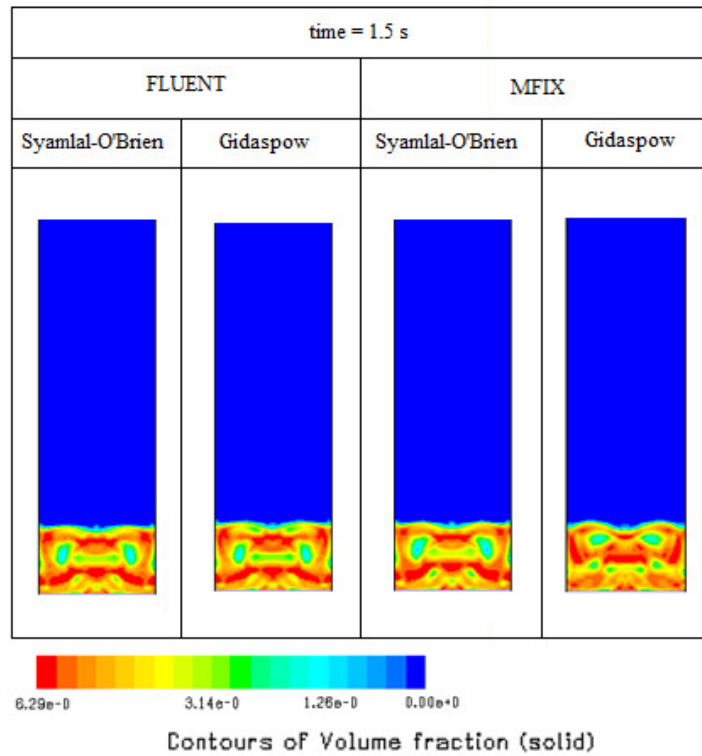


Figure 8.5: Snapshots of solid-phase vol. fraction for inflow velocity of 75 cm/s with spherical particles

The qualitative comparison is made in Fig. 8.6 by displaying some demonstrative snapshots from computational work and experiment at different times. While in the numerical simulation snapshots is appreciated the development of colliding and collapsing bubbles as the gas is being increasingly supplied at the bottom of the bed, the colors red and light blue indicate the volume fraction of solids in the fluidization domain, being red a high fraction of solid particles, while blue is the presence of air voids and bubbles forming in the bed. The experimental snapshots present a similar bubbling behavior, showing a high accurate qualitative comparison with respect to the numerical simulations. In both experiment and simulation it is observed that, beginning from a well mixing state, a series of bubbles starting to form at the bottom of the bed and colliding at the top, the bubble formation increases with higher gas flow as time progresses. Realistic agreement between experiment and simulation can be obtained from this comparison.

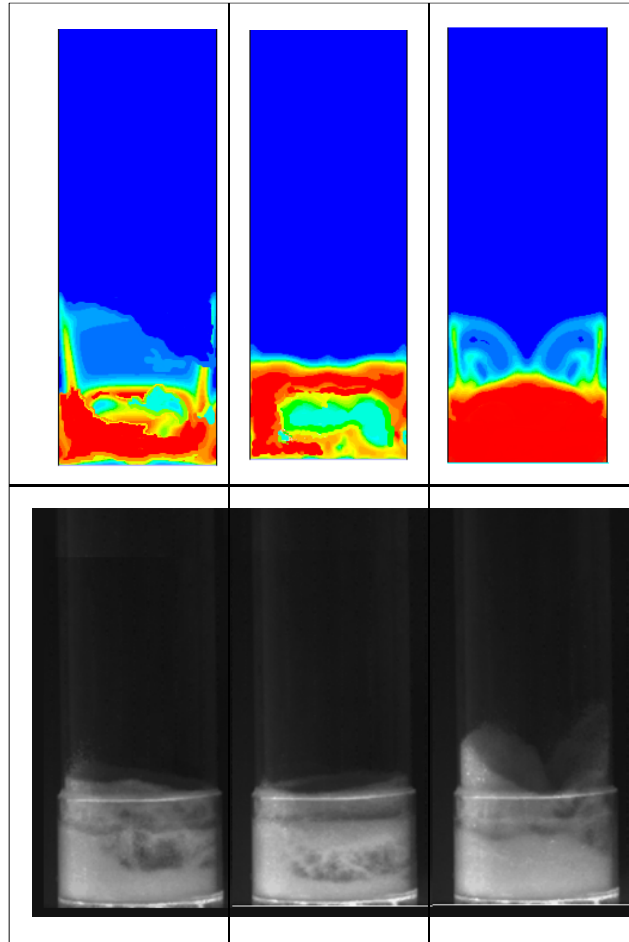


Figure 8.6: Comparison of snapshots of bubbling behavior of spherical particles among simulation (top row) and experiment (bottom row) at $t= 2, 5, 7$ s from left to right

8.2 Non-Spherical Particles

8.2.1 Literature Drag Correlation

On the other hand, another set of simulation was performed in order to obtain results and predictions for non-spherical particles. The pressure drop variation inside the bed as the superficial gas velocity increases using the Hölzer and Sommerfeld drag model is shown in Fig. 8.7, where both numerical values for FLUENT and MFIX are compared with the experimental and theoretical findings. The plot describes a typical fluidized bed behavior. Where a linear increase of pressure with respect to superficial velocity is seen, also the pressure drop reaches a maximum pressure drop value, furthermore, this pressure drop value remains near continuous showing a relative linear trend with increasing gas velocity once the fluidization point has been reached, however as the inflow gas velocity increases it reaches a point where pressure drop slightly increases once again.

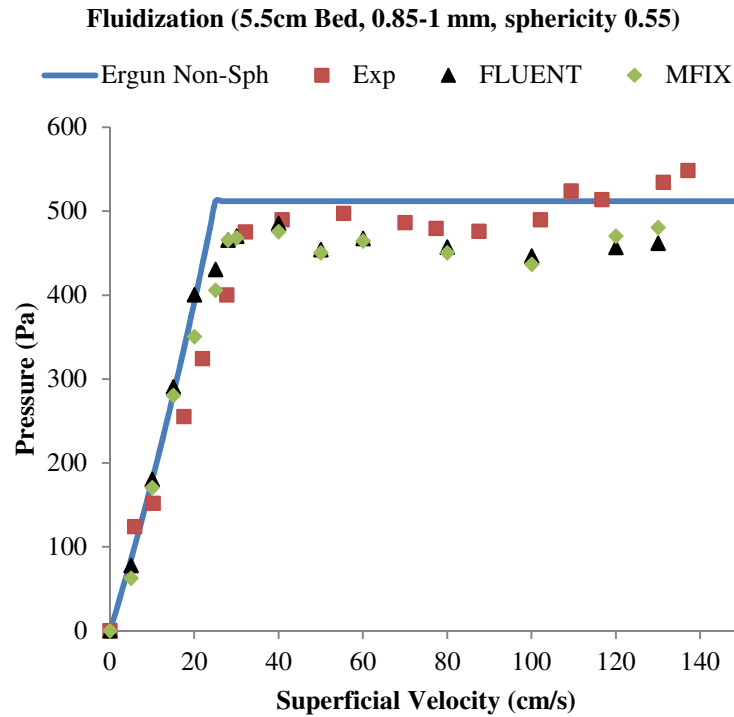


Figure 8.7: Non-spherical particles fluidization curves from simulations results, theoretical approximation and experimental predictions

As appreciated in Fig. 8.7, both FLUENT and MFIX drag models describe this behavior accurately, showing a good agreement with the experimental findings. As a result the non-spherical behavior differs from the spherical one at higher inflow velocity values, particularly showing a significant difference with respect to the theoretical non-spherical predictions. Table 6 shows results for non-spherical particles, the results deviate from Ergun equation for less than 10%.

Table 6: Non-spherical numerical, theoretical and experimental results

FLUENT		
Drag Correlation	Min. Fluidization Velocity (cm/s)	Pressure Drop (Pa)
Hölzer-Sommerfeld	31.0	480.2
MFX		
Drag Correlation	Min. Fluidization Velocity (cm/s)	Pressure Drop (Pa)
Hölzer-Sommerfeld	28.0	475.0
THEORETICAL		
Correlation	Min. Fluidization Velocity (cm/s)	Pressure Drop (Pa)
Ergun	26.52	512.0
EXPERIMENTAL		
Min. Fluidization Velocity (cm/s)		Pressure Drop (Pa)
32.41		476.0

Lastly, to provide a more precise understanding about the fluidization hydrodynamics, instantaneous gas and solid flow contours were recorded from within FLUENT and MFIX for non-spherical particles. Flow fields of the axial component of gas velocity at simulated flow time of 1.5 s are given in Fig. 8.8. Bubbling bed behavior is observed as the flow develops through the gas void between the solid particles. Also, the solid-phase velocity vectors are shown in Fig. 8.9 and a very good agreement between FLUENT and MFIX and numerical results is appreciated. In addition, Fig. 8.10 shows the solids volume fraction profile for inflow velocity of 75 cm/s at 1.5 s simulation time, no significant pattern differences exist among the gas volume fraction contours shown in FLUENT and MFIX. Numerical results of MFIX and Fluent are comparable.

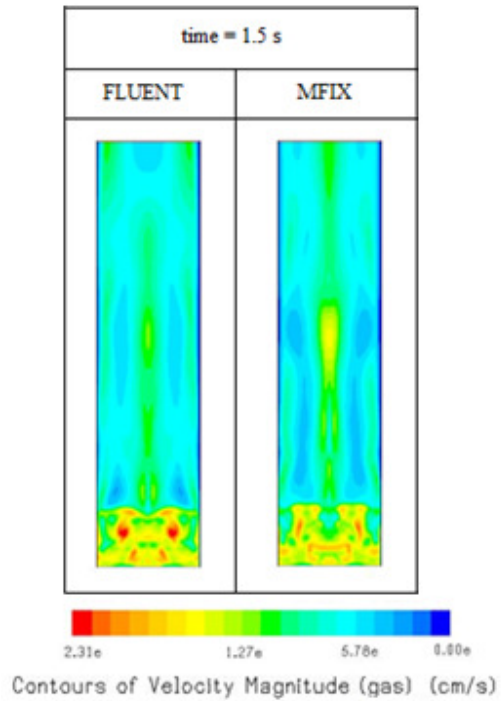


Figure 8.8: Snapshots of gas-axial velocity at 75 cm/s inflow velocity with non-spherical particles

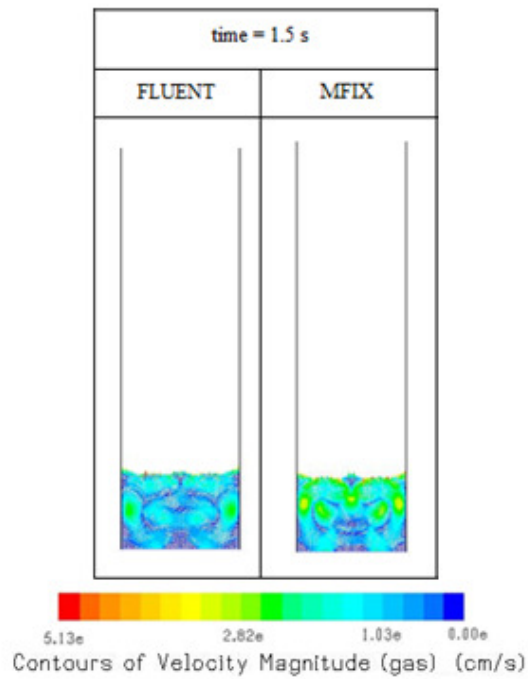


Figure 8.9: Snapshots of solids velocity vector-field for inflow velocity of 75 cm/s with non-spherical particles

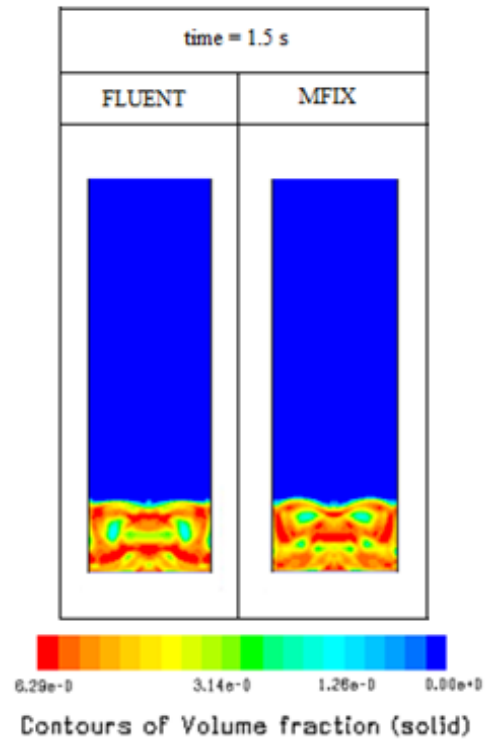


Figure 8.10: Snapshots of solid-phase vol. fraction for inflow velocity of 75 cm/s with non-spherical particles

8.2.2 Single Non-Spherical Particle Analysis

A. Numerical

In order to validate the model, particle velocity results were obtained using FLUENT, and contrasted with those found in Eqn. (6.8). Figure 8.11 shows the particle velocity plot, a 2% error was found between numerical results compared with those found by the theoretical calculation for terminal velocity. Figure 8.12 presents contours of velocity for the particle at different times.

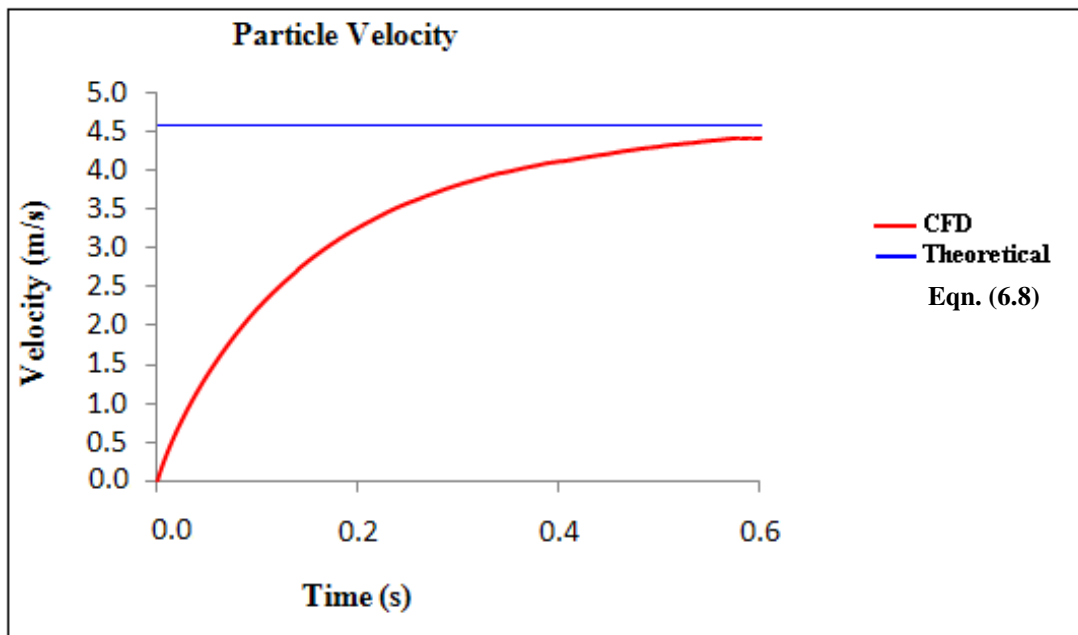


Figure 8.11: Particle velocity results

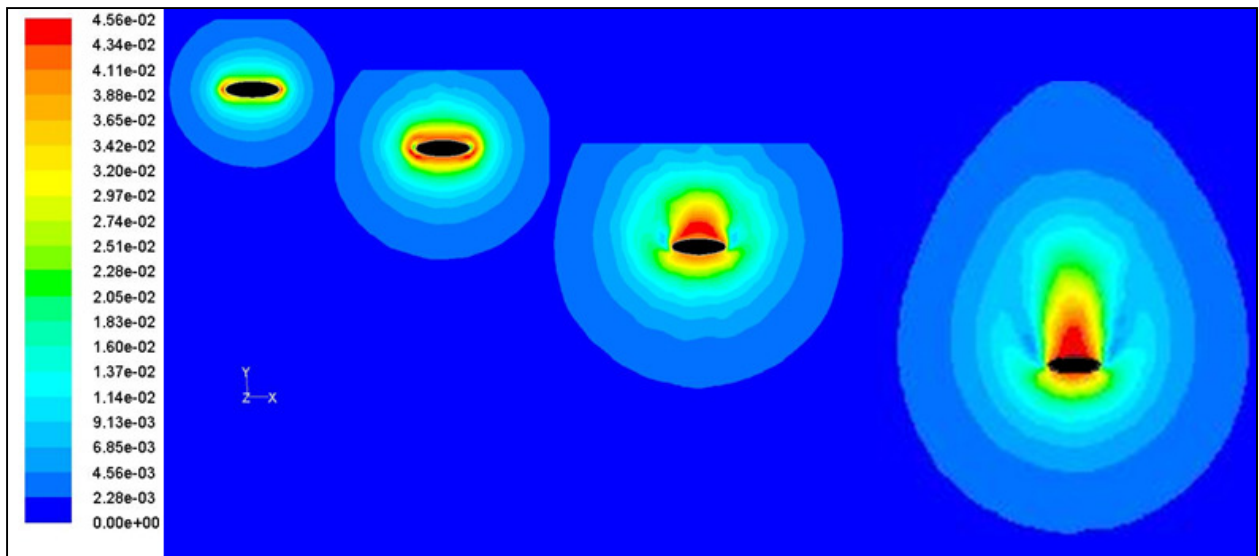


Figure 8.12: Velocity contours at different times

Figure 8.13 displays the force acting on the particle at the free-falling conditions, a fluctuation is observed due to the vortices acting on the particle.

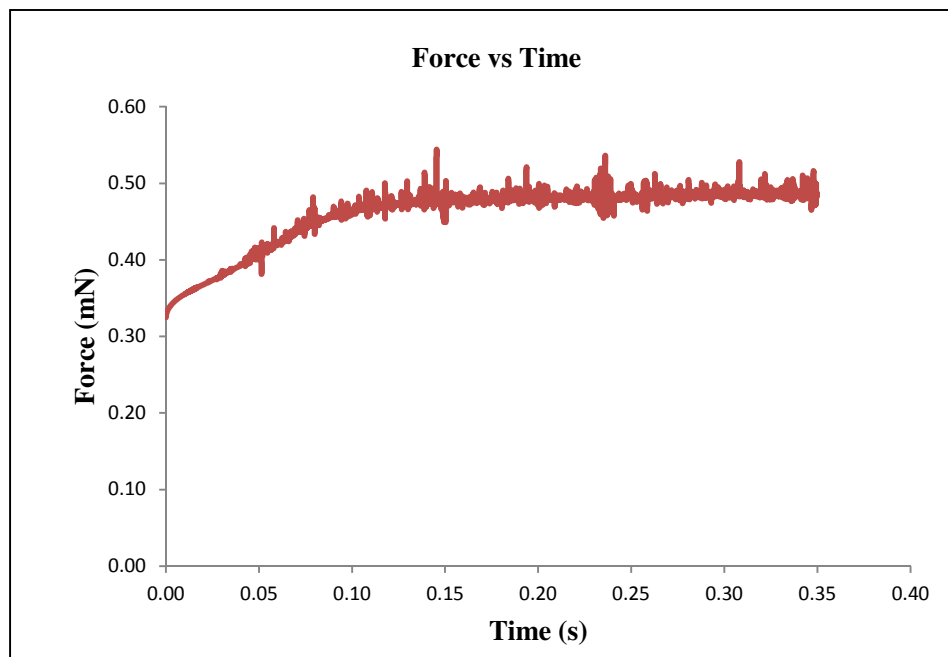


Figure 8.13: Fluid force acting on the particle

Equations (6.9-10) were used to calculate the particle drag coefficient at terminal velocity, a comparison between numerical and experimental results can be appreciated in Table 7:

Table 7: Numerical and experimental results comparison

Results	Numerical	Experimental
Re	1058	1081
Cd	0.52	0.58

B. Experimental

The initial terminal velocity for determining the approximate particle travel distance was calculated. The camera frame length traveled by a single particle, presented in Figure 7.4, was measured using an mm scale. After obtaining the travel time, the particle terminal velocity was obtained using Eq. (7.1). The terminal velocity for the present experiment was found to be approximately 4.7 m/s. The drag coefficient based on the measurement was determined experimentally using Eqn. (7.2) and was found to be approximately 0.58. The experimental uncertainty was also calculated based on a Student's t-distribution with a 95% confidence interval and estimated to be approximately 10% of the mean value presented.

8.2.3 Experimental Non-Spherical Drag Correlation

In order to develop a correlation of drag coefficient as a function of Reynolds number for non-spherical particles of a sphericity 0.55, experimental data was performed as described in previous sections, and 93 experimental data points were recorded for $Re < 1000$, as presented in the Appendix.

By considering the general drag correlation proposed described in Eqn. (6.14), this relationship is used in order to fit the non-spherical experimental data previously termed in this work. As a consequence, a non-linear least squares numerical technique is performed in conjunction with a Newton-

Raphson iterative scheme and the following equation is developed fitting the non-spherical experimental data:

$$C_D = \frac{24}{Re} (1 + 0.8943 Re^{0.3952}) + \frac{4.3215}{1 + \frac{160.1567}{Re}} \quad (8.1)$$

Figure 8.14 describes the drag coefficient vs. Reynolds number, for both the experimental data and the correlation found through non-linear fit.

Finally, the goodness of fit of Eqn. (8.1) is quantified using the RMS deviation. RMS deviation measures the average fractional displacement of the measured C_D values from the correlation line:

$$RMS = \sqrt{\frac{\sum_{i=1}^n (\log_{10}(C_{D_exp}) - \log_{10}(C_{D_cal}))^2}{n}} \quad (8.2)$$

Where the RMS values for this correlation is equal to 0.048.

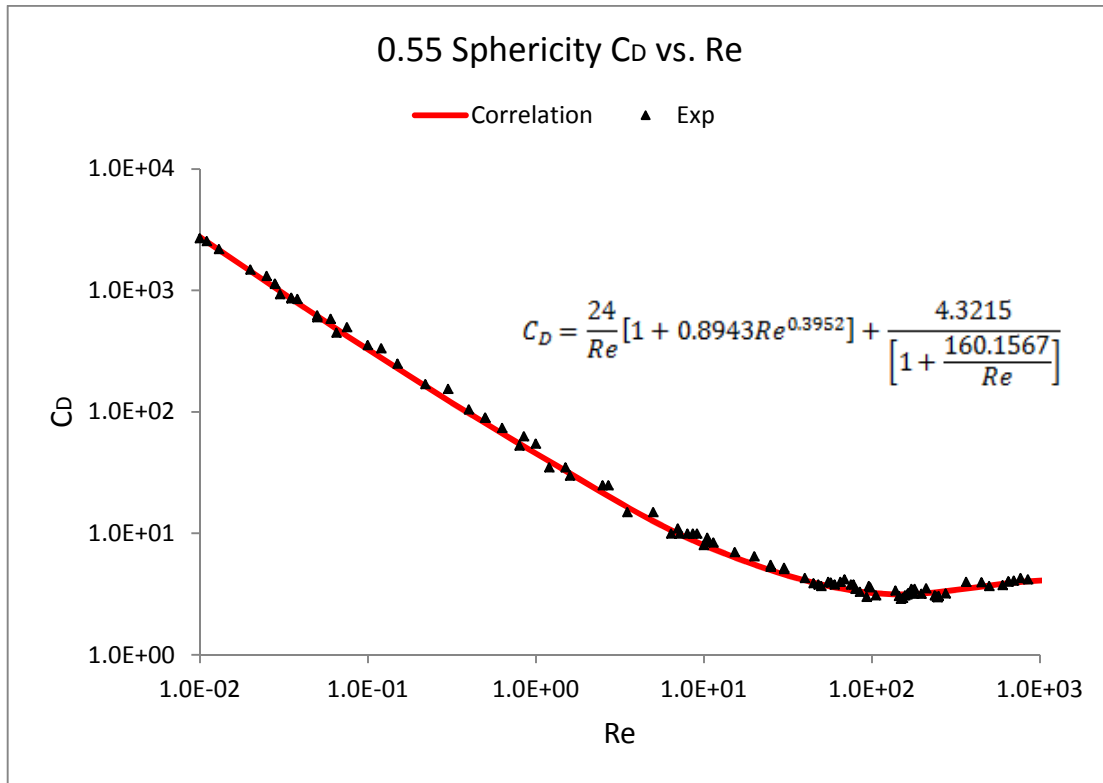


Figure 8.14: Drag coefficient vs. Reynolds number of non-spherical particles with sphericity of 0.55 (93 data points) and its corresponding numerical correlation

Furthermore, the fluidization of non-spherical particles is performed next, by using this experimentally developed drag correlation. First, by using Eqn. (5.5), the Syamlal-O'Brien drag correlation as baseline, the drag coefficient was changed from that of Eqn (5.6), Dalla Valle to the one numerically found through the fit given by Eqn. (8.1). Next, for this CFD non-spherical analysis a modification to the codes (FLUENT and MFIX) was made in order to take into account the newly developed non-spherical drag correlation. Both codes only deal with drag correlations designed for spherical particles. Thus a sub-routine written in C++ language was implemented into the Codes. The non-spherical drag correlation sub-routine is described in the Appendix.

The results acquired by the CFD codes describe a bubbling behavior in the fluidized bed that takes place in a transitory way, where splitting and collapsing of bubbles occur, due to this, fluctuations in the pressure drop are anticipated. In line to this, area-weighted average values of pressure drop values are recorded providing a comparison between simulation results. Consequently, time-averaging was carried out over a range of 1–10 seconds of time computation. The simulations was performed using FLUENT with non-spherical particles, the pressure drop variation inside the bed as the superficial gas velocity increases is shown in Fig. 8.15, where numerical values are compared with the experimental and theoretical findings. The plot describes a typical fluidized bed behavior. Where a linear increase of pressure with respect to superficial velocity is seen, also known as packed-bed behavior, until the inflow gas velocity reaches what is known as the minimum fluidization velocity U_{mf} , also the pressure drop reaches a maximum pressure drop value, theoretically this maximum pressure drop value should be equal to the weight of the bed per cross-sectional area of the vessel containing the particles.

Additionally, this pressure drop value remains near continuous showing a relative linear trend with increasing gas velocity once the fluidization point has been reached. As appreciated in Fig. 8.15, MFIX results describe with good accuracy the packed-bed behavior with respect to the theoretical

and experimental results as well, where a linear increase of pressure with respect to superficial velocity is appreciated, reaching later on the minimum fluidization velocity. In addition, this pressure drop value remains nearby constant showing a comparative linear development with increasing gas velocity, as seen before with the FLUENT results. By further increasing the inflow velocity the established constant pressure drop starts to fluctuate, due to the constant bubbling behavior of the bed. At this instance, FLUENT and MFIX numerical results describe somewhat smaller values than the experimental results for both numerical codes.

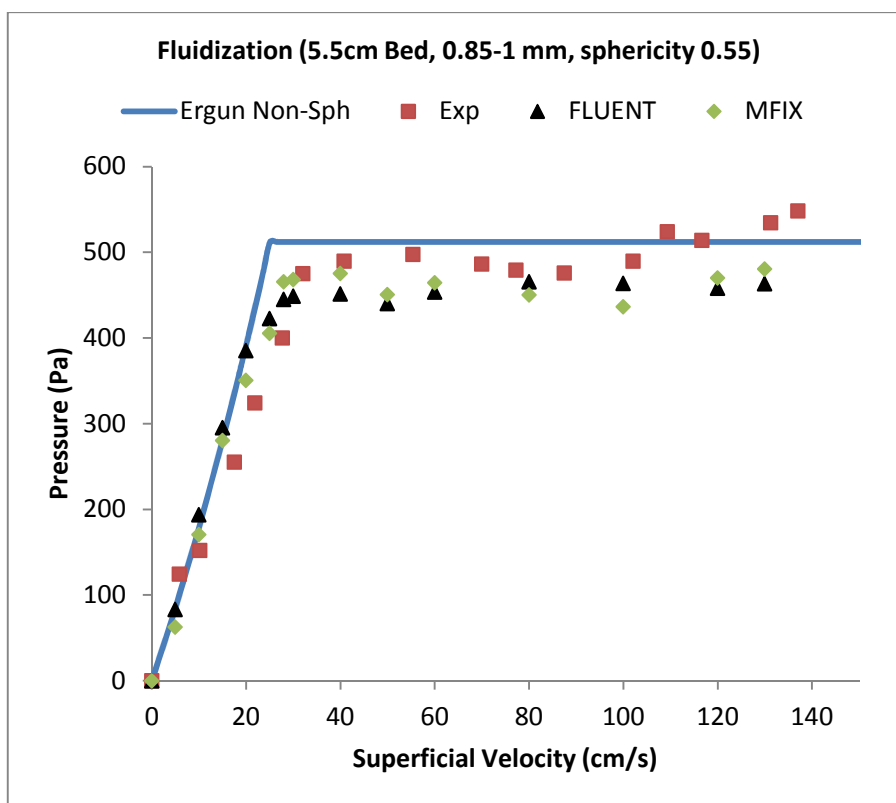


Figure 8.15: Non-spherical particles fluidization curves from simulations results, theoretical approximation and experimental predictions

The validation of the model with non-spherical particles was done in several steps. The numerical codes were tested for numerical convergence. The methods were stable and converged with

the set time step size. The fluid-particle interaction was compared with empirical solutions and experimental observations. Table 8 demonstrates the very good agreement of the measured pressure drop through a fluidized bed (at packed conditions no particle movement is observed since the flow speed is below the minimum fluidization velocity) with the predictions of Ergun's empirical equation and the experimental findings for non-spherical particles. The results deviate from Ergun equation for less than 10%.

Table 8: Non-spherical numerical, theoretical and experimental results

FLUENT	
Min. Fluidization Velocity (cm/s)	Pressure Drop (Pa)
30.5	450.5
MFX	
Min. Fluidization Velocity (cm/s)	Pressure Drop (Pa)
31.0	463.2
THEORETICAL	
Min. Fluidization Velocity (cm/s)	Pressure Drop (Pa)
26.52	512
EXPERIMENTAL	
Min. Fluidization Velocity (cm/s)	Pressure Drop (Pa)
32.41	476

In order to provide a more precise understanding about the fluidization hydrodynamics, instantaneous gas and solid flow contours were recorded from within FLUENT and MFX. Flow fields of the axial component of gas velocity at simulated flow time of 1.5 s are given in Fig. 8.16 for non-spherical particles. Bubbling bed behavior is observed as the flow develops through the gas void between the solid particles, both codes show similar behavior. Also, the solid-phase velocity vectors are shown in Fig. 8.17 and a very good agreement between FLUENT and MFX numerical results is

appreciated. In addition, Fig. 8.18 shows the solids volume fraction profile for inflow velocity of 75 cm/s at 1.5 s simulation time, no significant pattern differences exist among the gas volume fraction contours shown in between FLUENT and MFIX.

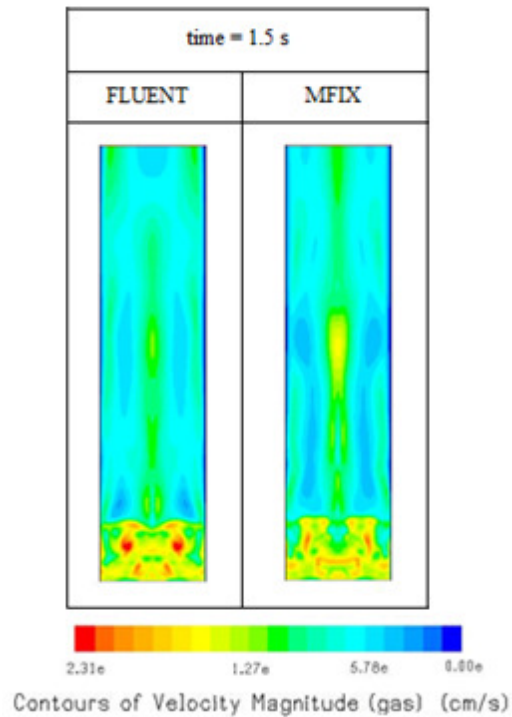


Figure 8.16: Snapshots of gas-axial velocity at 75 cm/s inflow velocity with non-spherical particles

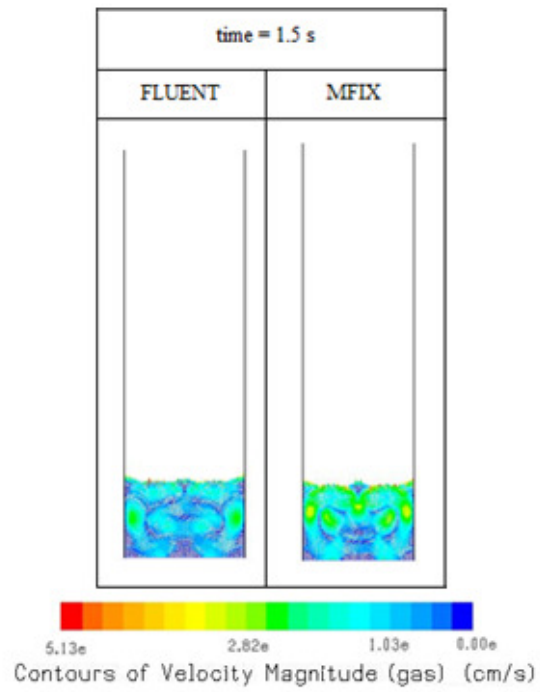


Figure 8.17: Snapshots of solids velocity vector-field for inflow velocity of 75 cm/s with non-spherical particles

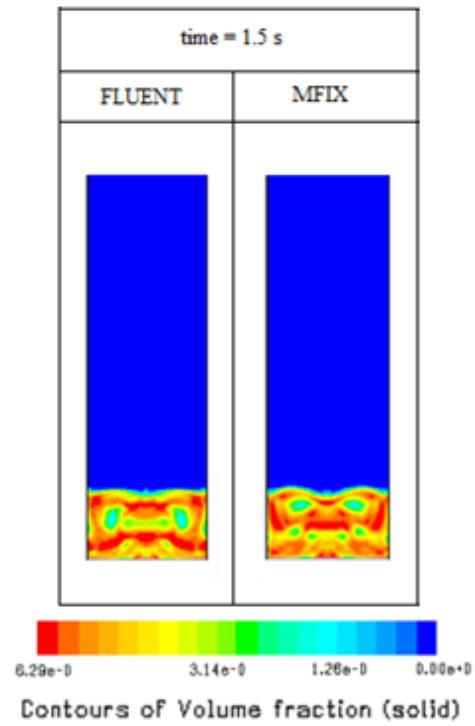


Figure 8.18: Snapshots of solid-phase vol. fraction for inflow velocity of 75 cm/s with non-spherical particles

Chapter 9: Conclusions

This study established a predictive method by which the hydrodynamics of a 2D fluidized bed can be documented for both spherical and non-spherical particles. This investigation offers an experimental study and simulation of multiphase flow in a fluidized bed. The behavior of spherical drag models, specifically the Syamlal-O'Brien and Gidaspow models on CFD numerical modeling of a 2D fluidized bed is investigated. Two CFD codes are used: the commercial software FLUENT and the open-source MFIX, developed by the DOE. MFIX and FLUENT results are compared between themselves for gas inflow velocities up to 130 cm/s. Also, the simulation of fluidized bed behavior with non-spherical particles is carried out. First, the Hölzer and Sommerfeld drag law found in literature is used for studying non-spherical particles. The non-spherical particles are developed by crushing bigger particles. Both spherical and non-spherical particle fluidizations curves are presented in this work. For the spherical particles portion of the investigation, the FLUENT code numerical results show a deviation less than 1.5% between the Gidaspow and Syamlal-O'Brien spherical drag laws, also less than 2% deviation with respect to the Ergun theoretical equation. MFIX results are found to be between the 2.5 % deviation with respect to the Ergun equation. Moreover, both FLUENT and MFIX codes correlate within 3% deviation with experimental findings. For the literature non-spherical drag law study, deviation is found for both pressure drop and minimum fluidization velocity. As for the FLUENT results with respect to Ergun equation a 6% is found for pressure drop while 17% for minimum fluidization velocity. MFIX has a 7% deviation for pressure drop and 5.6% for minimum fluidization velocity. If it is now compared the error found between experimental and numerical results, it is found that FLUENT deviation is 0.8% for pressure drop and 4.3% for minimum fluidization velocity. MFIX has a 0.2 % and 13.6% for pressure drop and minimum fluidization velocity. Thus, for this portion of the study the numerical results have a better correlation with those found experimentally rather than the theoretical non-spherical Ergun equation.

Moreover, the calculation of drag coefficient of a single solid non-spherical particle moving at the terminal velocity is studied. The numerical approximations were done using FLUENT. The non-spherical particle shape simulated in this study is a rice grain shaped as an ellipsoid. Experimental drag results are compared to experimental data for validation. The experimental setup is comprised of an elliptical rice particle and a high-speed camera system, with a capacity up to 500 kHz, used to record particle movement in the free falling stream to determine the terminal velocity of the rice grain. Drag coefficient is successfully modeled through CFD methodologies; in addition the numerical work is validated with an experimental method developed specifically for these measurements. The deviation between numerical and experimental work is less than 7 %.

Finally, this study established an experimental simple correlation formula for the standard drag coefficient of arbitrary shaped particles is established using a large number of experimental data specifically recorded for this work. This new correlation formula accounts for the particles sphericity (shape coefficient) of 0.55 over an entire range of Reynolds numbers up to the critical Reynolds number ($Re < 1e03$). The numerically fit drag correlation has a RMS deviation of 0.048 with respect to the drag experimental measurements. In addition, such a correlation was used for CFD hydrodynamic modeling of a gas-solid fluidized bed with non-spherical particles in uniform flow. The same two CFD codes previously described are used to perform this analysis. Both CFD codes results were compared between themselves for gas inflow velocities up to 130 cm/s. Deviation was found for both pressure drop and minimum fluidization velocity. As for the FLUENT results with respect to non-spherical Ergun equation a 12% is found for pressure drop while 15% for minimum fluidization velocity. MFIX had 9% deviation for pressure drop and 16% for minimum fluidization velocity. If it is now compared the error found between experimental and numerical results, it is found that FLUENT deviation is 5.4% for pressure drop and 5.9% for minimum fluidization velocity. MFIX has a 2.7 % and 4.4% for pressure drop and minimum fluidization velocity. In conclusion, the numerical results have a

better correlation with those found experimentally rather than the theoretical non-spherical Ergun equation.

References

- Anderson, T.B and R. Jackson, R., “A Fluid Mechanical Description of Fluidized Beds”. I & EC Fundam., 1967.
- Black, D. L., “Experimental Investigation of Particle Dispersion with Spherical and Nonspherical Particles,” Dissertation, BYU (1997)
- Black, D. L., McQuay, M.Q., Bonin, M. P., “Laser-based Techniques for Particle-size Measurements: a Review of Sizing Methods and Their Industrial Application,” Prog. In Energy and Comb. Sci. (1995)
- Boggs, S., “Measurement of Roundness and Sphericity Parameters Using an Electronic Particle Size Analyzer,” Journal of Sedimentary Petrology, Vol. 37, No. 3, 1967, pp. 907-913.
- Bouillard J. X., Lyczowski R. Y. and Gidaspow D., 1989, “Porosity distributions in a fluidized bed with an immersed obstacle”, AIChE Journal, Vol. 35, 908
- Brucato, A., Grisafi, F., Montante, G., “Particle Drag Coefficients in Turbulent Fluids,” Chemical Engineering Science, Vol. 53, No 18, pp. 3295 – 3314 (1998)
- Campbell, C. “Rapid Granular Flows”, Annual Review of Fluid Mechanics 22, 1990, pp. 57.
- Choudhuri, A., Love, N. Investigation of Gas-Solid Fluidized Bed Dynamics with Non-Spherical Particles, Technical proposal- DOE Program Solicitation: DE-FOA-0000173, 2010.
- Cleary, P.W., “The effect of particle shape on simple shear flows”. Powder Technology 179, 2008, pp. 144-163.
- Cleary, P.W., Metcalfe, G., Liffman, K., “How well do discrete element granular flow models capture the essentials of mixing processes?”. Applied Mathematical Modeling 22, 1998, pp. 995–1008.
- Cleary, P.W., Metcalfe, G., “Quantitative comparison of mixing rates between DEM and experiment in a slowly rotating cylinder”. Proceedings of the World Congress on Particle Technology, vol. 4, 2002, pp. 550.

- Cleary, P.W., “Large scale industrial DEM modeling. *Engineering Computations* 21, 2004, pp. 169–204.
- Cleary, P.W., “Industrial particle flow modeling using discrete element method”. *Engineering Computations* 26 (6), 2009, pp. 698–743.
- Clift, R., Grace, J. R., Weber, M. E., “Bubbles, Drops, and Particles,” Academic Press, New York, 1978.
- Crowe C., Sommerfeld M., and Tsuji Y., “Multiphase flows with droplets and particles”, CRC Press, New York, 1998.
- Cundall, P.A. and Strack, O. D., “A discrete numerical model for granular assemblies”, *Geotechnique* 29, 1979, pp. 47-65.
- Dalla Valle, J.M. “Micromeritics”. Pitman, London, 1948.
- Dasgupta S., Jackson R., and Sundaresan S., “Developing Flow of Gas-Particle Mixtures in Vertical Ducts.” *Ind. Eng. Chem. Res.*, Vol. 36, 1997, pp. 3375
- Detamore M.S., Swanson M.A., Frender K.R., and Hrenya C.M., 2001, “A kinetic theory analysis of the scale up of circulating fluidized beds”, *Powder tech.*, Vol. 116, 190-203.
- Detamore, M.S.. "A kinetic-theory analysis of the scale-up of circulating fluidized beds", *Powder Technology*, 2001.
- Dolej's, V., Machac', I., “Pressure drop during the flow of a Newtonian fluid through a fixed bed of particles”. *Chemical Engineering and Processing* 34, 1995, pp. 1–8.
- Enwald, H., Peirano, E. and Almstedt, A.-E., “Eulerian two-phase flow theory applied to fluidization”, *International Journal of Multiphase Flow* 22, 1996, pp. 21.
- Escudie´ a, R., Epstein, N., Grace, J.R., Bia, H.T., “Effect of particle shape on liquid-fluidized beds of binary (and ternary) solids mixtures: segregation vs. mixing”. *Chemical Engineering Science* 61, 2006, pp. 1528–1539.
- Food and Agriculture Organization of the United Nations, “Wood Gas as Engine Fuel” <http://www.fao.org/docrep/t0512e/t0512e0a.htm>, accessed 09/15/10.

Fraige, F., Langston, P., Chen, G., “Distinct element modeling of cubic particle packing and flow”. Powder Technology 186, 2008, pp. 224–240.

Ganser, G. H., “A Rational Approach to Drag Prediction of Spherical and Nonspherical Particles,” Powder Technology, Vol. 77, 1993, pp. 143 – 152.

Gao, J., Xu, C., Lin, S., Tang, G. and Guo, Y., “Advanced model for turbulent gas-solid flow and reaction in FCC riser reactors”, AIChE J., 45, 1999, pp. 1095.

Geldart, D., “Types of gas fluidization”, Powder Technology, 7, 1973, pp. 285-292.

Gera, D., Gautam, M., Tsuji, Y., Kawaguchi, T. and Tanaka, Y., “Computer simulation of bubbles in large-particle fluidized beds”, Powder Technology 98, 1998, pp. 38.

Gidaspow, D., Bezburuah, R. and J. Ding, J., “Hydrodynamics of Circulating Fluidized Beds, Kinetic Theory Approach. In Fluidization VII”, Proceedings of the 7th Engineering Foundation Conference on Fluidization, 1992, pp. 75–82.

Glasser B.J., Sundaresan S., and Kevrekidis Y.G., "From Bubbles to Clusters in Fluidized Beds." Phys. Rev. Lett., Vol. 81, 1998, pp. 1849

Glasser, B.J. "From Bubbles to Clusters in Fluidized Beds", Physical Review Letters, 1998

Goldhirsch, I., “Rapid granular flows”, Annual Review of Fluid Mechanics 35, 2003, pp. 267.

Goldschmidt, M. J. V., Weijers, G. G. C., Boerefijn, R., and Kuipers, J. A. M., “Discrete element modelling of fluidised bed spray granulation”, Powder Technology 138, 2003, pp. 39.

Gupta, C.K., Sathiyamoorthy. D., “Fluid bed technology in materials processing”, CRC Press, 1999.

Haider, A., Levenspiel, O., “Drag Coefficient and Terminal Velocity of Spherical and Nonspherical Particles,” Powder Technology, Vol 58, 1989, pp. 63-70.

Hartman, M., Trnka, O., Svoboda, K., “Free Settling of Nonspherical Particles,” Ind. Eng. Chem. Res., Vol. 33, 1994, pp. 1979–1983.

Helland, E., Occelli, R. and Tadrist, L., “Numerical study of cluster formation in a gas-particle circulating fluidized bed”, *Powder Technology* 110, 2000, pp. 210.

He Tao, B., Wenqi, Z. “Discrete element method modeling of non-spherical granular flow in rectangular hopper”, *Chemical Engineering and Processing: Process Intensification*, CEP-5777-2010.

Hilton, J.E., Mason, L.R., Cleary, P.W. “Dynamics of gas–solid fluidized beds with non-spherical particle geometry”, *Chemical Engineering Science* 65, 2009, pp. 1584–1596.

Hölzer, A., Sommerfeld, M., “New Simple Correlation Formula for the Drag Coefficient of Non-Spherical Particles”, *Powder Technology Journal*, Vol. 184, 2008, pp. 361-365.

Hoomans, B.P.B, Kuipers, J. A. M., Briels, W. J. and Swaaij, W. P. M. V., “Discrete particle simulation of bubble and slug formation in a two-dimensional gas-fluidised bed: a hardsphere approach”, *Chemical Engineering Science* 51, 1996, pp. 99.

Hoomans, B.P.B, Kuipers, J. A. M., Briels, W. J. and Swaaij, W. P. M. V., “Granular dynamics simulation of segregation phenomena in bubbling gas-fluidized beds”, *Powder Technology* 109, 2000, pp. 41.

Howard, J.R, “Fluidized Bed Technology: principles and applications”, Adam Hilger, Bristol and New York, 1989.

<http://www.netl.doe.gov/technologies/coalpower/gasification/pubs/images/Tr6-8-1.jpg>, accessed 09/16/10.

Jakobsen, Hugo A., "Fluidized Bed Reactors", *Chemical Reactor Modeling*, 2008.

Kawaguchi, T., Tanaka, T., and Tsuji, Y., “Numerical simulation of two-dimensional fluidized beds using the discrete element method (comparison between two- and three-dimensional models)”, *Powder Technology* 96, 1998, pp. 129.

Klett, J. D., “Orientation Model for Particles in Turbulence,” *J. of Atmos. Sci.*, Vol. 52, 1995, pp. 2276 –2285.

Kuipers, J.A.M. and van Swaaij, W.P.M., “Computational Fluid Dynamics Applied to Chemical Reaction Engineering”, *Adv. Chem Eng.*, 24, 1998, pp. 227.

Li, J., Kuipers, J.A.M., Effect of pressure on gas-solid flow behavior in dense gas-fluidized beds: a discrete particle simulation study, *Powder Technology* 127, 2002, pp. 173.

Li, Jie and Kuipers, J.A.M., Gas-particle interactions in dense gas-fluidized beds, *Chemical Engineering Science*, Vol. 58, 2003, pp711-718.

Li, S. "Modelling of the behaviour of gas-solid two-phase mixtures flowing through packed beds", *Chemical Engineering Science*, 200603.

Limtrakul, S., Chalermwattanatai, A., Unggerawirote, K., Tsuji, Y., Kawaguchi, T. and Tanthapanichakoon, W., “Discrete particle simulations of solids motion in a gas-solid fluidized bed”, *Chemical Engineering Science* 58, 2003, pp. 915.

Liu, B., Zhang, X., Wang, K., Hong, H., “Fluidization of non-spherical particles: sphericity, Zingg factor and other fluidization parameters”. *Particuology* 6, 2008, pp. 125–129.

Liu, L., Litster, J., “The effect of particle shape on the spouting properties of non-spherical particles”. *Powder Technology* 66, 1991, pp. 59–67.

Mikami, T., Kamiya, H. and Horio, M., “Numerical Simulation of Cohesive Powder Behavior in a Fluidized Bed”, *Chemical Engineering Science* 53, 1998, pp. 1927.

Ogawa, S., Umemura, A. and Oshima, N., “On the Equation of Fully Fluidized Granular Materials”. *J. Appl. Math. Phys.*, 1980, pp. 31-483.

Ouyang, J. and Li, J. “Particle-motion-resolved discrete model for simulating gas-solid fluidization”, *Chemical Engineering Science* 54, 1999, pp. 2077..

Renzo, A.D. and Maio, F.P.D., “Comparison of Contact-Force Models for Simulation of Collisions in DEM-Based Granular Flow Codes”, *Chemical Engineering Science* 59, 2004. pp. 525.

Richardson, J.R and W. N. Zaki, W.N., “Sedimentation and Fluidization: Part I”. Trans. Inst. Chem. Eng., 32, 1954, pp. 35–53.

Rhodes, M.J., Wang, X. S., Nguyen, M., Stewart, P. and Liffman, K., “Study of Mixing in Gas Fluidized Bed Using a DEM Model”, Chemical Engineering Science 56, 2001, pp. 2859.

Rhodes, M.J. and Wang, X.S., “The Role of Interparticle Force in Determining Geldart Group Behavior: a DEM Study”, AIChE Annual Meeting, 2000.

Rhodes, M.J., Wang, X. S., Nguyen, M., Stewart, P. and Liffman, K. “Use of discrete element method Simulation in Studying Fluidization Characteristics: Influence of Interparticle force”, Chemical Engineering Science 56, 2001, pp. 69-76.

Rhodes, M.J., Wang, X.S., Nguyen, N., Stewart, P., and Liffman, K., “Onset of cohesive behavior in gas fluidized beds: a numerical study using DEM simulation”, Chemical Engineering Science 56, 2001, pp. 4433-4438.

Samuelsberg, A.E. and Hjertager, B.H., “Computational Fluid Dynamic Simulation of an Oxy-Chlorination Reaction in a Full-Scale Fluidized Bed Reactor”, Proceedings of the 5th Int. Conf. Circulating Fluidized beds, Beijing (China), May 28- June 1, 1996.

Sinclair, J.L., “Hydrodynamic modeling in Circulating Fluidized Beds”, J R Grace, A Auidan, and T M Knowlton, Editors, 1997, Chapman and Hall: Great Britain.

Swamee, P. K., Ojha, C. S. P., “Drag Coefficient and Fall Velocity of Nonspherical Particles,” Journal of Hydraulic Engineering, Vol. 117, 1991, pp. 660-667.

Syamlal, M. “The Particle-Particle Drag Term in a Multiparticle Model of Fluidization”. National Technical Information Service, Springfield, VA, 1987. DOE/MC/21353-2373, NTIS/DE87006500.

Syamlal, M., Rogers, W. and O’Brien T. J. MFIx Documentation: Volume 1, Theory Guide. National Technical Information Service, Springfield, VA, 1993. DOE/METC-9411004, NTIS/DE9400087.

- Syamlal, M. and O'Brien, T.J. "Computer Simulation of Bubbles in a Fluidized Bed". AIChE Symp. Series, 85:22–31, 1989.
- Tsuji Y., Kawaguchi T., and Tanaka T., "Discrete Particle Simulation of Two Dimensional Fluidized Bed", Powder Tech., Vol. 77, 1993, pp. 79-87.
- Tsuji Y., Tanaka T., and Ishida T., "Lagrangian Simulation of Plug Flows of Cohesionless Particles in a Horizontal Pipe", Powder Tech., Vol. 71, 1993, pp. 239-250.
- Trang-Cong, S., Gay, M., Michaelides, E., "Drag Coefficients of Irregularly Shaped Particles", Powder Technology, Vol. 139, 2003, pp. 21-32.
- Van Wachem, B.G.M. and Almstedt, A.E., "Methods for multiphase computational fluid dynamics", Chemical Engineering Journal 96, 2003, pp. 81.
- Van Wachem, B. G. M., Van Der Schaaf, J., Schouten, J. C., Krishna, R., Van Den Bleek, C. M., "Experimental Validation of Lagrangian-Eulerian Simulations of Fluidized Beds", Powder Technology 116, 2001, pp. 155-165.
- Vogel, W., "Glass Chemistry", 2nd ed., Springer-Verlag Berlin and Heidelberg GmbH & Co. K, Germany, 1994.
- Wu, W.Y. "Hydrodynamic characteristics of a magnetically stabilized air fluidized bed of an admixture of magnetic and non-magnetic particles", Powder Technology, 1997.
- Xu, B.H. and Yu, A.B., "Numerical Simulation of the Gas-Solid Flow in a Fluidized Bed by Combining Discrete Particle Method with Computational Fluid Dynamics", Chemical Engineering Science 52, 1997, pp. 2785-2809.
- Xu, B.H., Yu, A.B., Chew, S.J., and Zulli, P., "Numerical Simulation of Gas-Solid Flow in a Bed with Lateral Gas Blasting", Powder Technology 109, 2000, pp. 13.
- Yuu, S., Umekage, T., and Johno, Y., "Numerical Simulation of Air and Particle Motions in Bubbling Fluidized Bed of Small Particles", Powder Technology 110, 2000, pp. 158.

Zhou, H., Flamant, G., Gauthier, D., and Flitiris, Y., “Simulation of Coal Combustion in a Bubbling Fluidized Bed by Distinct Element Method”, Chemical Engineering Research and Design 81, 2003, pp. 1144.

Appendix

Table 9: User Defined Function for Syamlal-Obrien with Holzer and Sommerfeld Drag Correlation

```
#include "udf.h"
#include "sg_mphase.h"

# define pi 4.*atan(1.)
#define diam2 1.e-3

DEFINE_EXCHANGE_PROPERTY(custom_drag_syam, cell, mix_thread, s_col, f_col)
{
  Thread *thread_g, *thread_s;
  real x_vel_g, x_vel_s, y_vel_g, y_vel_s, abs_v, slip_x, slip_y,
      rho_g, rho_s, mu_g, reyp, afac,
      bfac, void_g, vfac, fdrgs, taup, k_g_s;

  /* find the threads for the gas (primary) and solids (secondary phases).
  These phases appear in columns 2 and 1 in the Interphase panel respectively*/

  thread_g = THREAD_SUB_THREAD(mix_thread, s_col); /*gas phase*/
  thread_s = THREAD_SUB_THREAD(mix_thread, f_col); /* solid phase*/

  /* find phase velocities and properties*/

  x_vel_g = C_U(cell, thread_g);
  y_vel_g = C_V(cell, thread_g);

  x_vel_s = C_U(cell, thread_s);
  y_vel_s = C_V(cell, thread_s);

  slip_x = x_vel_g - x_vel_s;
  slip_y = y_vel_g - y_vel_s;

  rho_g = C_R(cell, thread_g);
  rho_s = C_R(cell, thread_s);

  mu_g = C_MU_L(cell, thread_g);

  /*compute slip*/
  abs_v = sqrt(slip_x*slip_x + slip_y*slip_y);

  /*compute reynolds number*/

  reyp = rho_g*abs_v*diam2/mu_g;

  /* compute particle relaxation time */

  taup = rho_s*diam2*diam2/18./mu_g;

  void_g = C_VOF(cell, thread_g); /* gas vol frac*/

  /*compute drag and return drag coeff, k_g_s*/

  afac = pow(void_g,4.14);
```

```

if(void_g<=0.85)
    bfac = 0.26*pow(void_g, 1.28);
else
    bfac = pow(void_g, 9.56872);

vfac = 0.5*(afac-0.06*reyp+sqrt(0.0036*reyp*reyp+0.12*reyp*(2.*bfac-
    afac)+afac*afac));
fdrgs = void_g*((24/sqrt(sphericity))+(3*sqrt(reyp))*(1/pow(sphericity,0.75)+
    (0.42*(pow(10,(0.4*(pow(-log(sphericity),0.2))))))* (reyp/sphericity))/
    (24.0*pow(vfac,2)));

k_g_s = (1.-void_g)*rho_s*fdrgs/taup;

return k_g_s;

```

Table 10: User Defined Function for Syamlal-Obrien Corrected with Experimentally Developed Drag Correlation

```

#include "udf.h"
#include "sg_mphase.h"

# define pi 4.*atan(1.)
#define diam2 1.e-3

DEFINE_EXCHANGE_PROPERTY(custom_drag_syam, cell, mix_thread, s_col, f_col)
{
    Thread *thread_g, *thread_s;
    real x_vel_g, x_vel_s, y_vel_g, y_vel_s, abs_v, slip_x, slip_y,
        rho_g, rho_s, mu_g, reyp, afac,
        bfac, void_g, vfac, fdrgs, taup, k_g_s;

    /* find the threads for the gas (primary) and solids (secondary phases).
    These phases appear in columns 2 and 1 in the Interphase panel respectively*/

    thread_g = THREAD_SUB_THREAD(mix_thread, s_col); /*gas phase*/
    thread_s = THREAD_SUB_THREAD(mix_thread, f_col); /* solid phase*/

    /* find phase velocities and properties*/

    x_vel_g = C_U(cell, thread_g);
    y_vel_g = C_V(cell, thread_g);

    x_vel_s = C_U(cell, thread_s);
    y_vel_s = C_V(cell, thread_s);

    slip_x = x_vel_g - x_vel_s;
    slip_y = y_vel_g - y_vel_s;

    rho_g = C_R(cell, thread_g);
    rho_s = C_R(cell, thread_s);

    mu_g = C_MU_L(cell, thread_g);

    /*compute slip*/
    abs_v = sqrt(slip_x*slip_x + slip_y*slip_y);

    /*compute reynolds number*/

    reyp = rho_g*abs_v*diam2/mu_g;

    /* compute particle relaxation time */

    taup = rho_s*diam2*diam2/18./mu_g;

    void_g = C_VOF(cell, thread_g); /* gas vol frac*/

    /*compute drag and return drag coeff, k_g_s*/

    afac = pow(void_g,4.14);

    if(void_g<=0.85)

```

```

    bfac = 0.26*pow(void_g, 1.28);
else
    bfac = pow(void_g, 9.56872);

    vfac = 0.5*(afac-0.06*reyp+sqrt(0.0036*reyp*reyp+0.12*reyp*(2.*bfac-
        afac)+afac*afac));
    fdrgs =
void_g*((24/reyp)*(1+0.8943*pow(reyp,0.3952))+(4.3215/(1+(160.1567/reyp))))/
    (24.0*pow(vfac,2));

    k_g_s = (1.-void_g)*rho_s*fdrgs/taup;

return k_g_s;

```

Table 11: MFIX DAT File Example

```
#
# Fluidized Bed Simulation
#
# Mario A. Ruvalcaba          11-05-12
#
# Run time for F90 allocatable arrays on Octane -- 3.3 h
# Run-control section
#
  RUN_NAME = 'Fluidized-Bed'
  DESCRIPTION = 'Fluidized Bed Simulation'
  RUN_TYPE = 'new'
  UNITS = 'cgs'
  TIME = 0.0      TSTOP = 1.0      DT = 1.0E-3      DT_MIN = 1.0E-12
  NORM_G = 0.0d0   NORM_S = 0.0d0   MAX_NIT = 30
  DISCRETIZE = 9*2
  ENERGY_EQ = .FALSE.
  SPECIES_EQ = .FALSE.      .FALSE.
#
# Physical Parameters
#
  UR_FAC(1) = 0.5

! Geometry Section

  COORDINATES      = 'cartesian'
  XLENGTH          = 12.0          !X length
  IMAX             = 160           !cells in i direction
  YLENGTH          = 50.0          !height
  JMAX             = 220           !cells in j direction

  NO_K             = .TRUE.        !2D, no k direction

  GRAVITY = 980

#
# Gas-phase Section
#
  MU_g0 = 1.8E-4
  MW_avg = 29.
#
# Solids-phase Section
#
  DRAG_TYPE = 'SYAM_OBRIEN'
  Drag_c1 = 0.26
  Drag_d1 = 9.56872
  RO_s    = 2.23
  D_p0    = 0.1

  e        = 0.8
  Phi      = 0.0
  EP_star  = 0.35
```

```

#
# Initial Conditions Section
#
      !           Bed           Freeboard
IC_X_w      =    0.0           0.0
IC_X_e      =   12.0          12.0
IC_Y_s      =    0.0           5.5
IC_Y_n      =    5.5          50.0

IC_EP_g     =    0.35          1.0

IC_U_g      =    0.0           0.0
IC_V_g      = @ (45.8/0.45)    45.8

IC_U_s(1,1) =    0.0           0.0
IC_V_s(1,1) =    0.0           0.0

IC_P_star   =    0.0           0.0
IC_T_g      =   300.0          300.0

#
# Boundary Conditions Section
#
      !           Inlet        Outlet
BC_X_w      =    0.0          0.0
BC_X_e      =   12.0          12.0
BC_Y_s      =    0.0          50.0
BC_Y_n      =    0.0          50.0

BC_TYPE     =    'MI'         'PO'

BC_EP_g     =    1.0

BC_U_g      =    0.0
BC_V_g      =   100.0

BC_P_g      = 1.013E6    1.013E6
BC_T_g      =   300.0

#
# Output Control
#
RES_DT = 0.01
      !
      ! EP_g P_g      U_g  U_s  ROP_s      T_g  X_g
      !      P_star  V_g  V_s              T_s1 X_s      Theta  Scalar
      !      W_g  W_s              T_s2
SPX_DT = 0.01 0.1      0.1  0.1  100.      100. 100.      100.0 100.0

NLOG      = 100
full_log = .true.

```

Table 12: Experimental Drag Coefficient and Reynolds Number Data

Re	C _{D-exp}	C _{D-cal}	(Log(C _{D-exp})-Log(C _{D-cal})) ²
0.010	2700	2747.77	5.80E-05
0.011	2550	2510.11	4.69E-05
0.013	2200	2142.90	1.30E-04
0.020	1490	1428.68	3.37E-04
0.025	1323	1159.81	3.27E-03
0.028	1140	1043.72	1.47E-03
0.028	1135	1043.72	1.33E-03
0.030	934	978.95	4.17E-04
0.035	874	848.74	1.62E-04
0.035	865	848.74	6.80E-05
0.038	850	786.69	1.13E-03
0.050	625	611.39	9.14E-05
0.050	602	611.39	4.52E-05
0.060	586	517.67	2.90E-03
0.065	450	481.34	8.55E-04
0.075	500	422.82	5.30E-03
0.100	355	326.40	1.33E-03
0.120	335	277.38	6.72E-03
0.150	250	227.61	1.66E-03
0.220	170	162.73	3.61E-04
0.300	155	124.46	9.08E-03
0.400	105	97.37	1.07E-03
0.500	90	80.65	2.27E-03
0.500	90	80.65	2.27E-03
0.630	74	66.49	2.16E-03
0.800	53	54.59	1.64E-04
0.850	63	51.94	7.03E-03
1.0	55	45.49	6.80E-03
1.2	35	39.25	2.48E-03
1.5	35	32.84	7.69E-04
1.6	30	31.20	2.88E-04
2.5	25	22.00	3.09E-03
2.7	25	20.73	6.61E-03
3.5	15	17.01	2.98E-03
5.0	15	13.04	3.70E-03
6.4	10	10.90	1.40E-03
7.0	11	10.23	1.01E-03
7.2	10	10.02	1.02E-06

8.0	10	9.31	9.70E-04
8.6	10	8.85	2.80E-03
9.1	10	8.51	4.88E-03
10.0	8.00	7.99	5.77E-07
10.5	9.20	7.73	5.73E-03
10.7	8.50	7.63	2.19E-03
11.4	8.40	7.32	3.58E-03
15.3	7.00	6.07	3.85E-03
20.0	6.50	5.19	9.62E-03
25.0	5.50	4.61	5.92E-03
25.0	5.30	4.61	3.70E-03
30.0	5.20	4.23	8.12E-03
30.0	5.10	4.23	6.67E-03
40.0	4.30	3.77	3.27E-03
45.0	3.90	3.63	9.84E-04
48.0	3.80	3.56	7.94E-04
50.0	3.70	3.52	4.55E-04
55.0	4.00	3.44	4.25E-03
57.0	3.95	3.42	3.97E-03
60.0	3.80	3.38	2.56E-03
65.0	4.00	3.34	6.22E-03
69.0	4.20	3.31	1.08E-02
75.0	3.80	3.27	4.18E-03
78.0	3.80	3.26	4.39E-03
80.0	3.50	3.26	9.88E-04
85.0	3.30	3.24	5.90E-05
93.0	3.00	3.23	1.03E-03
96.0	3.70	3.23	3.52E-03
98.0	3.60	3.23	2.27E-03
106.0	3.10	3.23	3.01E-04
138.0	3.40	3.26	3.13E-04
145.0	3.05	3.28	9.72E-04
149.0	2.90	3.28	2.93E-03
153.0	2.95	3.29	2.28E-03
158.0	3.10	3.30	7.55E-04
163.0	3.15	3.31	4.79E-04
165.0	3.23	3.32	1.33E-04
171.9	3.50	3.33	4.60E-04
175.0	3.30	3.34	2.46E-05
178.5	3.20	3.35	3.72E-04
180.0	3.50	3.35	3.69E-04
197.5	3.20	3.39	5.99E-04
211.0	3.53	3.41	2.11E-04

237.0	3.10	3.47	2.35E-03
243.0	3.02	3.48	3.76E-03
247.0	2.98	3.49	4.63E-03
250.0	3.05	3.49	3.44E-03
275.0	3.21	3.54	1.77E-03
365.0	4.00	3.67	1.36E-03
450.0	3.98	3.77	5.33E-04
500.0	3.70	3.82	1.97E-04
600.0	3.75	3.90	2.87E-04
650.0	4.02	3.93	9.42E-05
650.0	4.05	3.93	1.67E-04
700.0	4.10	3.96	2.30E-04
770.0	4.30	3.99	1.03E-03

Vita

Mario Alberto Ruvalcaba was born on December 19th, 1984 in Juarez, MEXICO. The eldest son of Mario Ruvalcaba and Lilia Andrade, he graduated from COBACH #6 High School in Juarez, MEXICO in Spring 2002 and joined The University of Texas at El Paso (UTEP) to pursue a Bachelor of Science in Mechanical Engineering. After the completion of his Bachelor Degree in Fall 2007 he worked as a CFD engineer at Delphi Automotive Systems, at the same time he began attendance in the same university to pursue a Master Degree in Mechanical Engineering. He started working at the Combustion and Propulsion Research Laboratory under the supervision of Dr. Ahsan Choudhuri, where the facilities few years later became the Center for Space Technology Research where he currently performs.

Mario Alberto Ruvalcaba obtained his Master degree in Mechanical Engineering in Summer 2009. Eventually he enrolled in the Engineering Doctoral program working towards his PhD in Energy Science and Engineering. Ruvalcaba has been the recipient of various honors and awards including the Artemio de la Vega Memorial Scholarship and the State of Texas Public Education Grant (TPEG) for International Students. While pursuing his degree, Ruvalcaba's research was focused on the CFD modeling of multiphase flow problems such as gas-solid fluidization technologies. Mario Alberto Ruvalcaba has presented his research at international conference meetings and workshops including the 2011 Annual International Energy Conversion Engineering Conference in San Diego, CA.

Permanent address: 1320 Smith St. #206
Logansport, IN 46947

This dissertation was typed by Mario Alberto Ruvalcaba